ACS APPLIED MATERIALS & INTERFACES

www.acsami.org

Research Article

Reaction Mechanism of Electrodeposited ε-MnO_2: A Proton-Centered Pathway in Aqueous Zn-Ion Systems

Varun R. Kankanallu, Adesanmi Adeniyi, Jianming Bai, Lu Ma, Hui Zhong, Xianghui Xiao, Zhongshu Ren, Steven Ehrlich, Jorge Moncada, Akhil Tayal, Eli Stavitski, Xiao Tong, Kenneth J. Takeuchi, Amy C. Marschilok, Esther S. Takeuchi, Mingyuan Ge, and Yu-chen Karen Chen-Wiegart*

Cite This: *ACS Appl. Mater. Interfaces* 2026, 18, 26078−26094

Read Online

ACCESS | Metrics & More | Article Recommendations | Supporting Information

ABSTRACT: Aqueous Zn/MnO_2 batteries have garnered significant interests owing to their abundance, high theoretical specific capacity, safety, and low cost. However, large-scale application of these systems is limited by the incomplete understanding of the MnO_2 reaction chemistry. The different crystal lattice structures among MnO_2 polymorphs contribute to the variations in reported reaction mechanisms. Among them, ε-MnO_2 polymorph, the dominant phase in electrolytic manganese dioxide (EMD), is notably observed during the charge cycles of aqueous Zn/MnO_2 batteries. In this work, we investigate the electrochemical behavior of an ε-MnO_2 cathode synthesized via electrodeposition from a $ZnSO_4$ and $MnSO_4$ electrolyte, onto a 3-dimensional carbon cloth substrate. Proton intercalation emerges as the dominant charge storage mechanism, critically enabling the reversibility of ε-MnO_2 during cycling, as revealed by operando synchrotron X-ray diffraction and X-ray absorption spectroscopy. Additionally, a proton-coupled dissolution/redeposition pathway operates alongside minor Zn^{2+} intercalation, as quantified by Rietveld refinement. Morphological and chemical heterogeneities are studied by transmission X-ray microscopy further validates this reaction mechanism. These mechanistic insights provide the foundation for rationally designing Zn/MnO_2 batteries with optimized proton dynamics and charge transfer, advancing these systems as a viable solution for safe, cost-effective grid-scale energy storage.

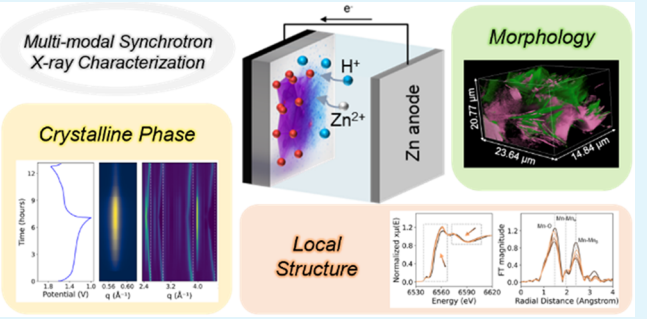

KEYWORDS: *electrolytic manganese dioxide (EMD), aqueous electrolyte, proton intercalation, dissolution-redeposition, operando X-ray diffraction, X-ray absorption spectroscopy, transmission X-ray microscopy*

1. INTRODUCTION

Rechargeable aqueous Zn-ion batteries (AZIBs) are a promising battery technology for large scale energy storage, and have garnered significant interests owing to Zn abundance, low cost, relatively low redox potential (−0.76 V vs standard hydrogen electrode), high theoretical specific capacity (820 mAh g^{-1}), and environmental friendliness.[1,2] Rational engineering of electrodes, electrolytes, and separators is a key factor that significantly influences the electrochemical performance of AZIBs.[3−6] The most frequently used cathodes for rechargeable AZIBs include vanadium-based compounds, manganese-based oxides, Prussian blue analogues organic compounds and defect-engineered heterostructures.[7−11] Among these cathode materials, manganese dioxide is particularly notable for its high theoretical capacity of 616 mAh/g enabled by a $2e^-$ redox process, as well as the environmental abundance and low cost of manganese compared to alternative materials.[12−14] Electrolytic MnO_2 (EMD) is predominantly used in commercial alkaline Zn/MnO_2 primary batteries due to its precisely controlled morphology and crystallinity, which enable more consistent and reliable battery performance.[15]

Manganese-based oxides as cathode materials for Zn/MnO_2 battery possesses the unique ability to exist in multiple valence states with diverse structural forms over a wide temperature range, where their polymorphs play a crucial role in guiding their reaction mechanism.[16,17] MnO_2 polymorphs including α-MnO_2 (2 × 2 tunnels), β-MnO_2 (1 × 1 tunnels), γ-MnO_2 (1 × 1 and 1 × 2 tunnels), ε-MnO_2 (1 × 1 and 1 × 2 tunnels), δ-MnO_2 (layered structure) and other manganese-based oxides including Mn_3O_4 (spinel structure) and $ZnMn_2O_4$ (spinel structure) have been explored as cathode materials for

Received: November 10, 2025
Revised: March 9, 2026
Accepted: April 13, 2026
Published: April 30, 2026

AZIBs.[18−24] Electrolytic MnO_2 (EMD) is the predominant polymorph used in alkaline Zn/MnO_2 primary batteries.[15] Its crystal structure is characterized by an intergrowth of ramsdellite and pyrolusite domains.[25]

Numerous reaction mechanisms have been proposed with the various MnO_2 polymorphs, yet there remains uncertainty regarding reversibility of the phase transitions, morphology influence on reaction pathways, and reaction kinetics in the neutral or mildly acidic aqueous electrolytes. In the Zn/β-MnO_2 system, a mechanism involving proton-mediated dissolution has been reported.[26,27] This process involves the formation of a zinc hydroxyl sulfate (ZHS) phase during discharge, followed by the redeposition of MnO_2 alongside a chalcophanite ($ZnMn_3O_7{\cdot}3H_2O$) phase during charge. Gao et al. reported the coinsertion of H^+/Zn^{2+} in the charge-storage mechanism of Zn/α-MnO_2 system, and attributed the capacity loss to the irreversible formation of spinel-structured $ZnMn_2O_4$ on the cathode.[28] Yuan et al. reported that Zn^{2+} insertion into the α-MnO_2 cathode is unlikely; instead, the charge storage mechanism is dominated by proton intercalation, as demonstrated through advanced electron microscopy, electrochemical analysis, and theoretical calculations in aqueous batteries.[29] Aguilar et al. reported that regardless of the initial phase, whether β-MnO_2 or γ-MnO_2, the ε-MnO_2 phase forms during the redeposition of MnO_2 in subsequent charging cycles.[30] Wang et al. confirmed the redeposition of the ε-MnO_2 phase from a pristine Mn_3O_4 cathode after subsequent charging in an aqueous mild electrolyte.[23] Regardless of solution concentration, current density, or substrate, the primary electrodeposited phase during charging is typically ε-MnO_2.[31] Hence, studying the reaction mechanism of the electrodeposited ε-MnO_2 phase is imperative to understanding the mechanism of the extended cycled MnO_2 cathodes in AZIBs.[31,32]

The electrochemical reduction mechanism of electrolytic MnO_2 has been extensively studied in the context of alkaline primary batteries for several decades. Kozawa and Yeager demonstrated that the cathodic reduction of EMD proceeds initially through proton insertion into the γ/ε-MnO_2 framework, leading to the formation of MnOOH (Mn^{3+}), followed by the electrochemical reduction of Mn^{3+} to soluble Mn^{2+} at deeper states of discharge which precipitates as $Mn(OH)_2$.[33] Chabre and Pannetier later provided a comprehensive structural and electrochemical review of the γ/ε-MnO_2 system, elucidating the intergrowth of ramsdellite and pyrolusite and highlighting the prominence of this proton-coupled reaction mechanism under nonrechargeable alkaline conditions.[34] In contrast to classical alkaline MnO_2 chemistries used predominantly in primary Zn/MnO_2 batteries, this work examines ε-MnO_2 as a cathode material operating in a neutral to mildly acidic aqueous $ZnSO_4$ electrolyte.

Synchrotron X-ray characterization techniques have been used as a powerful suite of tools to study battery materials, particularly AZIBs owing to their ability to provide real-time dynamic monitoring of the structural, chemical, and morphological evolution of the battery electrode, with high spatial and temporal resolution and a variety of contrast mechanisms, that surpass the capabilities of conventional X-ray techniques.[35−37] Synchrotron X-ray diffraction (XRD) and X-ray absorption spectroscopy (XAS) provide insights into the long-range and short-range order of the battery electrode, respectively, allowing for the examination of crystal structure, phase transitions, and chemical states of the formed phases during cycling. Synchrotron X-ray nanotomography with transmission X-ray microscopy provides 3D visualization of the internal microstructure changes, including expansion/contraction, dissolution/deposition, as well as crack propagation/formation of the continuously evolving battery electrodes at tens of nm resolution.[36,38] Combining these techniques as a multimodal synchrotron characterization approach, could enable complementary studies of the electrode material including diffraction, transmission, fluorescence, and spectroscopy data across a wide range of length scales, down to just few nanometers.[39,40]

In this study, ε-MnO_2 electrodes were synthesized via electrodeposition under controlled pH condition. The electrochemical discharge−charge cycling of the ε-MnO_2 electrode versus zinc metal was investigated in a mildly acidic Zn-based electrolyte to understand the reaction mechanism, utilizing a combination of advanced synchrotron techniques. The structural changes and phase transitions of the electrodeposited phases during cycling were studied with operando XRD, providing detailed information on how the crystal structure in materials evolves under operational conditions. The lattice parameter measurements and weight fraction quantification provide insights into potential cation intercalation and the underlying crystalline reaction mechanism. Furthermore, the local geometric and electronic structures were characterized to explore atomic interactions and oxidation state changes, using operando XAS to provide a deeper understanding of the behavior of the electrodes at the atomic level. The morphological evolution of the electrode, chemical heterogeneities during phase transitions, and charge transport limitations were examined using X-ray nanotomography and 2D X-ray Absorption Near Edge Spectroscopy (XANES) chemical imaging techniques. Finally, differential capacity analysis reveals the capacity contributions from different reaction domains, further advancing the fundamental understanding of this battery system.

2. RESULTS AND DISCUSSION

2.1. Structural Evolution via Operando X-ray Diffraction

The ε-MnO_2 cathode was synthesized via a constant-current electrodeposition process using an electrolyte composed of 1 M $ZnSO_4$, 0.5 M $MnSO_4$, and 0.1 M H_2SO_4 (Figure S1). The pH of the electrodeposition electrolyte was measured to be 1.2. During the electrodeposition of MnO_2, the current applied primarily drives the reduction of Mn^{2+} to MnO_2. The Mn−H_2O Pourbaix diagram (Figure S1) shows the thermodynamic stability of different manganese species and highlights the operating conditions that favor the deposition of MnO_2. Additionally, it has been shown that the formation of MnO_2 is kinetically more favorable in the $MnSO_4$ + H_2SO_4 electrolyte.[41] The addition of 0.1 M H_2SO_4 is crucial because it (i) maintains Mn^{2+} solubility by suppressing precipitation of hydroxide species and (ii) enforces a strongly acidic pH-potential regime where MnO_2 deposition is favored (consistent with the Mn−H_2O Pourbaix diagram in Figure S1). These conditions promote efficient MnO_2 deposition and, based on prior EMD literature, the formation of ε-polymorph MnO_2 during the electrodeposition process is kinetically favored.[41−43] A carbon cloth coated with multiwalled carbon nanotubes (MWCNTs) served as the working electrode, while Zn was used as the counter electrode. While parasitic side reactions, such as hydrogen evolution and chemical Zn dissolution may occur at the electrode, their extent is reduced due to the high Zn^{2+} concentration and the dominance of Zn plating at the

https://doi.org/10.1021/acsami.5c22636
ACS Appl. Mater. Interfaces 2026, 18, 26078−26094

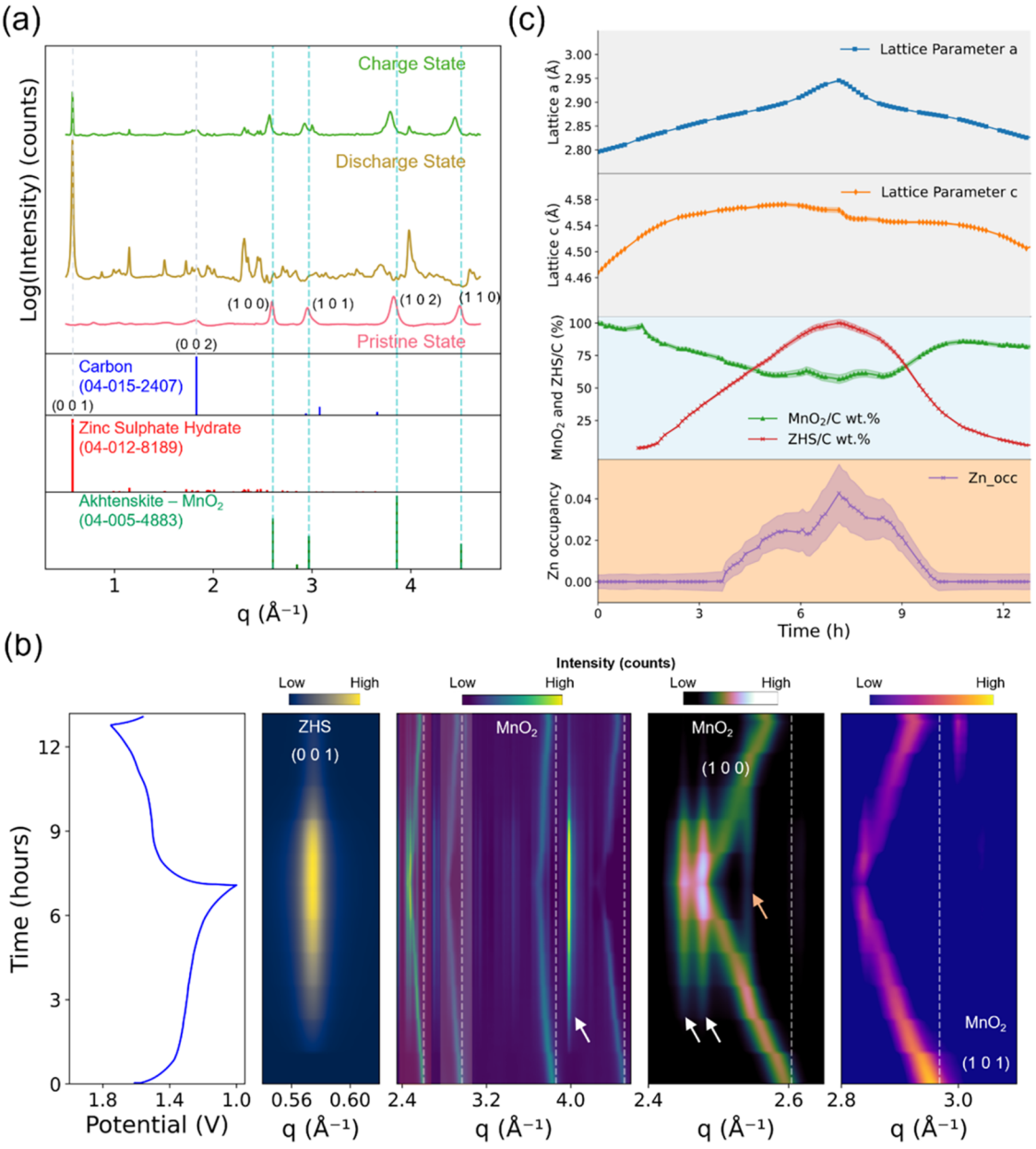

Figure 1. Structural evolution of the ε-MnO_2 electrode in 1 M $ZnSO_4$ electrolyte. (a) Operando XRD patterns of pristine, first-cycle discharge, and charge states. (b) Potential profiles and waterfall plots illustrate the evolution of the ZHS (001) plane, overview for ε-MnO_2 phase, and zoom-in view for (100) and (101) planes of ε-MnO_2 phase during operando X-ray diffraction. The orange arrow indicates a secondary peak. (c) Rietveld refinement results showing the gradual changes in lattice parameters a, c for ε-MnO_2 and the relative weight percentages of ε-MnO_2 and ZHS. The curve width reflects the one-sigma fitting uncertainty from the Rietveld analysis.

applied current densities. Further details on the synthesis are provided in the Section 4.

The structural characteristics of the synthesized material and its evolution in 1 M $ZnSO_4$ electrolyte were investigated using synchrotron XRD. In its pristine state, the electrode exhibits a densely packed hexagonal crystal structure, characteristic of the ε-polymorph of MnO_2. Compared to the standard ε-MnO_2 polymorph, the synthesized electrode shows a leftward peak shift in the XRD pattern (Figure 1(a)). Rietveld refinement of the XRD data for electrodeposited ε-MnO_2 reveals a small but measurable lattice expansion (a = 2.796 Å, c = 4.468 Å) compared to the standard values (a = 2.786 Å, c = 4.412 Å, PDF # 04−005−4883) (see Figure S2). Additionally, oxidation state and atomic % were estimated using X-ray photoelectron spectroscopy (XPS) (see Figure S3). The average oxidation state (AOS) of Mn centers in the electrodeposited MnO_2 polymorph was estimated based on the Mn 3s peak splitting energy (ΔBE) obtained from XPS, using the following empirical correlation (see eq 1)[44]

$$\text{AOS} = 8.95 - 1.13\Delta\text{BE (eV)} \quad (1)$$

The XPS Mn(3s) peak splitting (4.82 eV) corresponds to an oxidation state of +3.5. This nonstoichiometric value of oxidation state indicates the presence of cation vacancies in the MnO_2 structure, which can arise either from the missing Mn^{4+} in the lattice or the substitution of Mn^{4+} by Mn^{3+}.[45] The broad diffraction peaks could be the results of either the nanocrystalline character or microstrain of the material and XPS results

https://doi.org/10.1021/acsami.5c22636
ACS Appl. Mater. Interfaces 2026, 18, 26078−26094

indicate the defect-rich microstructure. Such structural imperfections naturally arise during electrodeposition, where rapid growth kinetics favor metastable, nonstoichiometric phases over the ideal ε-MnO_2 structure. These imperfections may also involve microtwinning, where multiple crystal domains share a common crystallographic plane, and De Wolff-type disorder, which reflects intergrowth between ramsdellite and pyrolusite domains. These structural faults create strain at the domain boundaries, which is relieved through the formation of manganese (cation) vacancies. To maintain charge neutrality, these manganese vacancies are primarily compensated by the reduction of neighboring Mn^{4+} to Mn^{3+}. This resulting high concentration of lower-valent Mn^{3+} can, in turn, promote the formation of oxygen vacancies as a secondary charge-balancing mechanism.[34] Based on the Reutschi formalism,[45] the chemical formula of the electrodeposited MnO_2 can be written as $Mn_{1-x-y}^{4+}Mn_y^{3+}\square_x O_{2-(4x+y-0.098)}Zn_{0.049}(OH)_{4x+y-0.098}$, where $\square$ denotes Mn vacancies. For simplicity, this compound is referred to as MnO_2 throughout the manuscript. Therefore, the as-synthesized are best described as EMD-like ε-MnO_2 with inherent structural disorder, rather than an idealized ε-MnO_2 polymorph, in line with the typical characteristics observed in the literature.[30,31]

To understand the structural evolution of the ε-MnO_2 polymorph in a mild aqueous electrolyte (1 M $ZnSO_4$), operando synchrotron X-ray diffraction was performed. As seen in XRD patterns measured at the end of the discharge and charge states (Figure 1(a)), the ε-MnO_2 peaks corresponding to the (100), (101), (102) and (110) planes shift to a lower q ($Å^{-1}$) during discharge, indicating lattice expansion (see the white dotted line in Figure 1(b)), followed by a partial return to pristine state upon charging. Simultaneously there is formation of the ZHS phase during discharge. In the charged state, the peaks remain slightly shifted to the left and do not completely return to their initial positions along with the residual presence of ZHS phase. ZHS is primarily detected through its characteristic (001) reflection, while higher-order ZHS peaks disappear due to partial dissolution and loss of long-range crystallinity. The persistence of the (001) peak reflects residual, surface-confined or highly disordered ZHS, which remains detectable due to its strong basal-plane scattering under operando conditions. The relative weight fraction of ZHS in the charged state was further estimated by Rietveld refinement of the operando X-ray diffraction data, confirming its presence as a minor residual phase. While the formation of ZHS is beneficial as a pH buffer, its physical deposition can also hinder reaction kinetics.

The uniform shift of multiple ε-MnO_2 reflections to lower q during discharge, followed by partial recovery upon charge, indicates reversible lattice expansion and contraction associated with the insertion and removal of H^+/H_3O^+ and/or Zn^{2+} ions within the ε-MnO_2 framework. Such behavior is characteristic of ion insertion-driven structural response rather than lattice strain or structural disorder. The evolution of these structural changes during discharge and charge is depicted in the waterfall plots (Figure 1(b)). Quantitative analyzes obtained through Rietveld refinement including lattice parameters, where the a-parameter represents the side length and the c-parameter corresponds to the height of the hexagonal ε-MnO_2 lattice are presented in Figure 1(c). Alongside this, the relative weight percentages of MnO_2 and ZHS, as well as Zn occupancy, are also shown, offering insights into the contributions of each component to the overall electrochemical capacity. The MnO_2 and ZHS weight percentages were normalized against the carbon current collector, which remains unchanged throughout the electrochemical cycle to account for the incident X-ray beam intensity fluctuation. The Rietveld refinement results corresponding to the discharge and charge states are provided Figure S2.

The ZHS phase, identified by its characteristic (001) diffraction plane, and by refining the structure using Rietveld refinement emerges during the discharge process and significantly diminishes upon charging, with a weak residual (001) reflection persisting due to partial dissolution and loss of long-range crystallinity. Within the q-range of 2.4−4.6 $Å^{-1}$, the ε-MnO_2 phase exhibits a gradual shift in peak position toward lower q-values during discharge and back to higher q-values during charging. The MnO_2 peak position is marked by a dotted line in Figure 1(b). During the initial stages of discharge, the sloping voltage profile coincides with a steep increase in the c-lattice parameter, indicating tunnel expansion to accommodate H^+ or Zn^{2+} intercalation. Rietveld refinement indicates that this process is dominated by proton insertion during the early discharge stage, with Zn^{2+} incorporation remaining negligible until the later stages of discharge. The overall change in the volume of the ε-MnO_2 active material is primarily driven by variations in the a-lattice parameter, which exhibits a more significant change compared to the c-parameter (see Figure S3).

Following this sloping region, the voltage decreases more gradually. Here, the c-parameter remains nearly constant while the a-parameter increases progressively, accompanied by a decline in the relative MnO_2 weight percentage. The absence of new diffraction peaks in this region suggests that ion insertion occurs within the vacant interstitial or tunnel sites of the ε-MnO_2 structure rather than forming new crystalline phases. Analysis of Zn occupancy reveals minimal tunnel site occupation until the later stages of discharge, with Zn occupancy peaking at ∼0.045 near the end of discharge. The shaded regions (or curve widths) in Figure 1(c) represent the corresponding one-sigma uncertainty ranges derived from the covariance matrix during refinement, indicating the confidence intervals for the fitted parameters.

The refined Zn occupancy of ∼0.045 from Rietveld analysis indicates that Zn incorporation into the ε-MnO_2 lattice during the initial discharge is limited. This observation is consistent with recent DFT simulations on various MnO_2 polymorphs (α, β, δ, and γ), which show that intercalation of H^+ has a lower thermodynamic energy barrier than Zn^{2+}, whereas proton diffusion exhibits a significantly higher kinetic barrier compared to Zn^{2+}.[46] As the MnO_2 electrode undergoes a discharge and charge process, we observe that the lattice parameters a and c (Figure 1c) do not fully return to their original state, indicating that the electrode structure evolves toward a more reduced state. These results suggest that, with continued electrochemical cycling and structural evolution, Zn^{2+} intercalation may become increasingly favorable as the electrode structure evolves. While Zn incorporation is initially limited, ongoing cycling and structural reorganization could enable greater Zn accommodation within the lattice. However, directly quantifying an increase in Zn^{2+} occupancy via common ex situ elemental analysis is confounded by the unavoidable presence of zinc-containing surface precipitates (ZHS), which makes it difficult to distinguish lattice-intercalated zinc from surface species. Therefore, future studies can further test this

https://doi.org/10.1021/acsami.5c22636
ACS Appl. Mater. Interfaces 2026, 18, 26078−26094

hypothesis by examining precycled electrodes with operando X-ray diffraction (XRD).

The concurrent decrease in MnO_2 weight percentage and negligible Zn occupancy during the early discharge stage suggests proton-mediated MnO_2 dissolution. This reduction in weight percentage is accompanied by consistent changes in the lattice parameters a and c, which can be attributed to proton insertion. A similar behavior is observed in TiO_2, where proton insertion is coupled with electron transfer.[47,48] Thermodynamic insights from the MnO_2 Pourbaix diagram indicate that MnO_2 tends to convert to Mn^{2+} in mild aqueous electrolytes, supporting the likelihood of proton-mediated dissolution.[49] However, the consistent lattice parameter a suggests that, in addition to dissolution, a proton insertion−coupled electron transfer mechanism is also active.

In summary, the cathode undergoes both reactions 2 and 3 during discharge.

$$xH_3O^+_{(aq)} + xe^- + MnO_{2(s)} \rightarrow H_xMnO_{2(s)} + xH_2O_{(aq)} \quad (2)$$

$$MnO_{2(s)} + 2H_2O_{(l)} + 2e^- \rightarrow Mn^{2+}_{(aq)} + 4OH^-_{(aq)} \quad (3)$$

The anode undergoes

$$Zn_{(s)} \rightarrow Zn^{2+}_{(aq)} + 2e^- \quad (4)$$

Near the end of discharge, a distinct splitting of the broad ε-MnO_2 (100) peak is observed in the q-range of 2.4−2.65 $Å^{-}$ (Figure 1(b)), with the main peak continuing to shift toward a lower q-value while a secondary peak emerges and diminishes in intensity, identified by an orange arrow in Figure 1(b). This secondary peak can be indexed to the primary diffraction peak of the $ZnMn_2O_4$ (Hetaerolite, PDF # 04−002−4954), corresponding to (211) peak contraction of 0.6% in q-value compared to the reference, suggesting either strain or nonstoichiometry in the formed phase. This peak reappears and strengthens during the corresponding charge phase, suggesting that the intercalated, disordered phase undergoes reversible dissolution and redeposition alongside the primary MnO_2 phase. The formation of the intercalation phase can be represented by eq 5, with the maximum value of y reaching ∼0.045.

$$H_xMnO_{2(s)} + yZn^{2+}_{(aq)} + 2ye^{-1} \rightarrow Zn_yH_xMnO_{2(s)} \quad (5)$$

The OH^- generated during reaction 3 induces a precipitation reaction near the cathode, as described by eq 6

$$4Zn^{2+}_{(aq)} + SO^{2-}_{4(aq)} + 6OH^-_{(aq)} + 5H_2O_{(l)} \rightarrow Zn_4SO_4(OH)_6\cdot 5H_2O_{(s)} \quad (6)$$

To evaluate local electrolyte effects, an analytical transport model (see Supporting Information) was developed to describe proton consumption at the MnO_2 cathode and the resulting interfacial alkalization. The model shows that this pH rise is buffered by the precipitation of ZHS, providing a mechanistic basis for the observed ZHS formation and the dominance of H^+ intercalation. This buffering by ZHS stabilizes the local pH and is critical for preventing runaway dissolution. During the subsequent charge, this ZHS layer also acts as a host for the redeposition of dissolved Mn^{2+}.[50] Throughout the discharge process, a 40% decrease in relative MnO_2 weight fraction is observed, contributing significantly to the capacity, along with a Zn occupancy of ∼0.045. Upon charging, the trend reverses: diffraction peaks for MnO_2 (100) and (101) planes shift back to higher q-values, and the intensity of the disordered phase increases. Additionally, a 20% recovery in the ε-MnO_2 weight fraction is observed, suggesting partial redeposition of the ε-MnO_2 phase. This behavior contrasts with our prior observations of β-MnO_2, where no peak growth was detected during the charge state,[27] supporting the conclusion that ε-MnO_2 is the more kinetically favored phase during redeposition.

Although the diffraction peaks largely return to their original positions upon full charge, only 20% of the MnO_2 phase is recovered, implying that the remaining material transforms into a less crystalline phase, which is examined further in this study using other techniques that are sensitive to noncrystalline phases. The progressive decrease in MnO_2 recovery with continued cycling is assessed semiquantitatively through differential capacity (dQ/dV) analysis, as shown in Figure 7. Additionally, the relative ZHS weight percentage decreases more sharply during the initial stages of the charging process, which is hypothesized to act as a precursor or substrate for the deposition of the layered Zn−Mn phase.[51] Notably, at the end of the charge state, a new peak appears at approximately 3.02 $Å^{-1}$, which is attributed to local disorder and intergrowth effects with in the ε-MnO_2 structure (see Figure 1(b)). No additional reflections indicative of layered birnessite, Zn-containing layered phases, spinel Mn_3O_4, or Mn_2O_3 are observed. The isolated nature, low intensity, and proximity of the ∼ 3.02 $Å^{-1}$ reflection to the ε-MnO_2 (101) peak strongly suggest that this feature arises from electrochemically induced disorder or locally distorted ε-MnO_2 domains, rather than the formation of a new crystalline phase.

While ion-exchange or pH-dependent approaches are used to probe proton insertion, in the present ε-MnO_2 system these methods predominantly reflect bulk electrolyte processes arising from concurrent dissolution−redeposition and buffering reactions and therefore do not provide a quantitative measure of lattice proton content. To confirm whether the observed lattice changes arise mainly from proton intercalation rather than Zn^{2+} insertion, an operando XRD experiment using heavy water (D_2O) as the solvent was conducted. Replacing H_2O with heavy water enables direct comparison of H^+ and D^+ behavior, where any isotope-dependent variations provide insight into the role of protons in the electrochemical process.

As shown in Figure 2, the operando XRD results reveal distinct lattice evolutions in ε-MnO_2 when cycled in H_2O and D_2O based 1 M $ZnSO_4$ electrolytes. During discharge, the a-lattice parameter ($\Delta a/a_0$, defined as $(a - a_0)/a_0$, where a_0 is the initial lattice parameter a prior to electrochemistry) in the D_2O system shows a slightly smaller overall expansion than in H_2O. The lattice parameters are obtained from operando XRD measurements during continuous galvanostatic cycling and therefore represent quasi-steady structural states under electrochemical cycling rather than fully relaxed equilibrium configurations. Consequently, the reduced lattice expansion in the D_2O system is attributed to slower D^+ insertion kinetics and a lower effective concentration of intercalated D^+ under current, consistent with the reduced discharge capacity observed in Figure 2(c). Likewise, the c-lattice parameter ($\Delta c/c_0$, defined as $(c - c_0)/c_0$, where c_0 is the initial lattice parameter c prior to electrochemistry) plateaus at a lower value, indicating milder distortion along the c-axis during D^+ insertion. The transient dip observed during early charging falls within the refinement uncertainty and reflects sensitivity to

https://doi.org/10.1021/acsami.5c22636
ACS Appl. Mater. Interfaces 2026, 18, 26078−26094

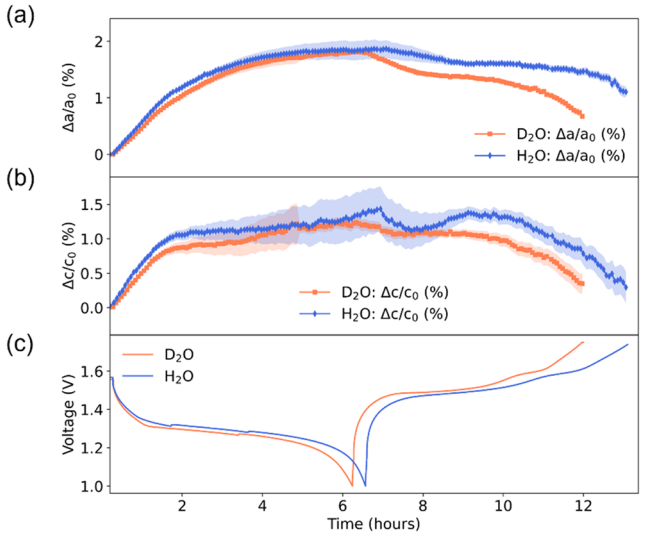

Figure 2. Comparison of lattice parameter evolution in ε-MnO_2 during operando XRD in 1 M $ZnSO_4$ electrolytes prepared with H_2O and D_2O. (a) Relative change in a-lattice parameter ($\Delta a/a_0$). (b) Relative change in c-lattice parameter ($\Delta c/c_0$). (c) Corresponding voltage profiles. The line width and shaded regions indicate the standard error from lattice-parameter refinement.

phase-fraction redistribution and partial loss of long-range order during rapid deintercalation, rather than a distinct structural transition.

Upon charging, the D_2O system exhibits a faster lattice contraction, attributed to the stronger D−O bonds that favor rapid resolvation once deintercalation begins.[52] The higher solvation energy of D^+ drives a faster extraction, while H^+ shows a more gradual and reversible relaxation. Together, these isotope-dependent differences demonstrate that proton (H^+/D^+) intercalation governs the observed structural evolution under operando conditions. Given the interplay between intercalation and dissolution, it is crucial to differentiate the capacity contributions from each process. To further investigate changes in oxidation state and local coordination under operando conditions, X-ray absorption spectroscopy (XAS) is employed.

2.2. Local Coordination Evolution via Operando X-ray Absorption Spectroscopy

During electrochemical cycling, changes in the local coordination environment were investigated using operando X-ray absorption spectroscopy (XAS) in transmission mode. The schematic in Figure 3(a) illustrates the cell orientation used for the measurements. To avoid interference with the phases forming on the electrode across the Mn K-edge, $MnSO_4$ was excluded from the electrolyte. Additionally, the cathode electrode was positioned in the same plane as the Zn foil anode, which further minimized the influence of changing Mn or Zn ion concentrations in the electrolyte in the operando XAS measurements in comparison with the stacked operando cell configuration.

The cell potential was plotted against time for the first four electrochemical cycles at a C-rate of 0.2C. The edge jump at the Mn and Zn K-edges, which corresponds to the amount of Mn and Zn present in the electrode, was determined by the difference between the postedge and pre-edge lines interpolated to the peak of the first derivative (E_0) (Figure 3(b)). A consistent increase and decrease in Mn content was observed, while Zn exhibited the opposite trend, indicating the bulk migration of Mn and Zn phases during electrochemical cycling. The variations in Mn and Zn concentrations follow the cell potential trend, with Zn accumulation becoming more prominent over successive cycles, as evident from the increasing baseline of the Zn signal, shown as a sloped dash line, in Figure 3(b).

To quantify the extent of cation intercalation into the active material, an accurate estimation of the Mn oxidation state is essential. Several methods, including the half-inflection point method, the peak of the first derivative, and the edge integral method, can be used for estimating the oxidation state by calibrating against standard oxidation states. Among these, the edge integral method provides the most accurate representa-

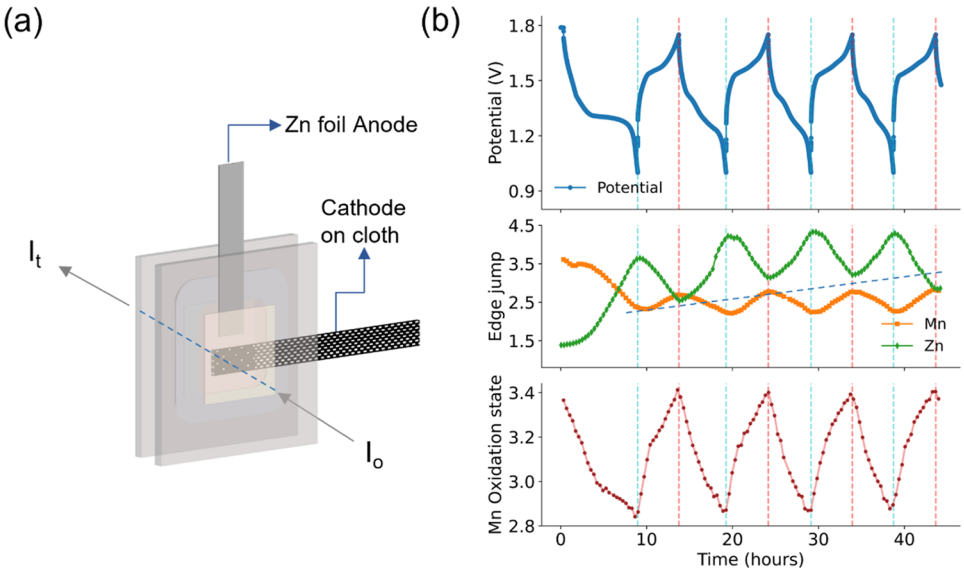

Figure 3. Operando X-ray absorption spectroscopy in transmission mode across the Mn and Zn K-edges of the ε-MnO_2 cathode in the Zn/ε-MnO_2 battery with 1 M $ZnSO_4$ electrolyte. (a) Schematic of the operando cell geometry used for measurements. (b) Mn and Zn K-edge jump signals correspond to the changes in the Mn and Zn phase concentrations and oxidation states during electrochemical cycling.

https://doi.org/10.1021/acsami.5c22636
ACS Appl. Mater. Interfaces 2026, 18, 26078−26094

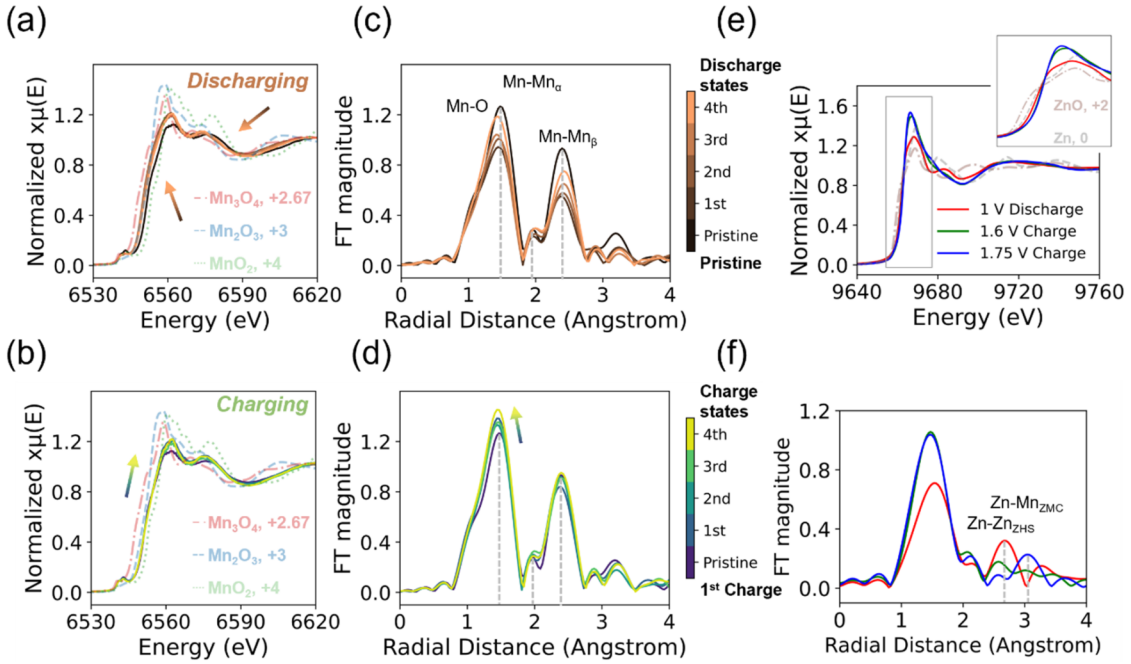

Figure 4. X-ray Absorption Spectroscopy of the operando and ex situ measurement across the Mn and Zn K-edges. (a, c) Mn K-edge spectra of the ε-MnO_2 cathode at the end of discharge states in energy space (a) and *R*-space (c) for the first four cycles. (b, d) Mn K-edge spectra at the end of charge states in energy space (b) and *R*-space (d) for the first four cycles. (e, f) Ex situ Zn K-edge spectra for pristine, discharged, 1.6 V charged, and fully charged states in energy space (e) and *R*-space (f).

tion of the Mn oxidation state, as it accounts for data averaging, thereby minimizing noise and errors.[53,54] The Mn oxidation state was estimated by using the edge integral method, as described in Section 4.

Initially, the Mn oxidation state was +3.37, which decreased to +2.84 after the first discharge, indicating a change of +0.53. This bulk-sensitive value is consistent with the surface-sensitive XPS-derived AOS of +3.5, as the variation reflects a combination of the inherent experimental uncertainties of the two techniques and a difference between the surface and bulk chemical states. This oxidation state change corresponds to a capacity of 162 mAh/g, calculated based on the theoretical capacity of 616 mAh/g for the Mn^{4+} to Mn^{2+} two-electron redox reaction. The overall discharge capacity during the first cycle was 295 mAh/g, with the difference attributed to active material MnO_2 dissolution.

Most of the oxidation state change occurs during the sloping region of the voltage profile, with only minor changes observed in the plateau region. This trend is also reflected in the synchrotron X-ray diffraction data, where the plateau region is primarily associated with capacity contributions from dissolution, suggesting that intercalation and dissolution do not occur simultaneously in this system.

The X-ray absorption near edge spectroscopy (XANES) analysis reveals variations in the end of discharged and charged states compared to the pristine state in energy space (Figure 4(a,b)). Notably, at the end of discharge and charge states exhibit similar spectral features in the XANES region, indicating reversibility of local structure of Zn/ε-MnO_2 battery.

The radial density function (*R*-space) obtained from extended X-ray absorption fine Structure (EXAFS) analysis provides insight into the local Mn coordination environment, showing the distribution of Mn−O, Mn−Mn$_\alpha$, and Mn−Mn$_\beta$ bonds (see Figure S4) for the first four cycles discharged and charged electrochemical states across the Mn K-edge. Changes in *R*-space (Figure 4(c)) indicate that Mn−O bond length decreases, while Mn−Mn$_\beta$ bond length increases in the discharged states. In the charged states, the EXAFS *R*-space function shows an increase in Mn−Mn$_\beta$ coordination, suggesting the buildup of charged species (Figure 4(d)).

The complete evolution of the XANES energy-space and EXAFS *R*-space during electrochemical cycling for the first cycle discharge and charge state is shown in Figure S5. During the discharge state, the XANES spectra shift toward lower energies, indicating a reduction in the Mn oxidation state. In the EXAFS region, a decrease in *R*-space intensity suggests increased structural disorder. Additionally, a slight decrease in the Mn−O bond length and an increase in the Mn−Mn$_\beta$ bond length is observed. During the charge state, a reverse trend is evident, indicating partial restoration of the original structure.

Since the material also facilitates Zn intercalation, it contributes to the complex phase formation in the system. However, operando data alone does not provide an accurate estimate of Zn incorporation due to the high concentration of $ZnSO_4$ in the electrolyte. To overcome this limitation, ex situ measurements were performed at specific discharged and charged states.

The XANES spectra shows that the first cycle discharge state differs significantly from the first cycle 1.6 and 1.75 V charged samples (see Figure 4(e)). In energy space, the 1.6 and 1.75 V charged samples exhibit similar features, with their absorption edges slightly shifted to the right of the ZnO standard indicating a more oxidized Zn state (see inset in Figure 4(e)). To further investigate this, the EXAFS region was analyzed, and the *R*-space radial density function was plotted (see Figure 4(f)). The first peak observed around 1−2 Å, corresponds to the Zn−O coordination complex. In the discharged state, a peak appears between 2.5−3 Å, which corresponds to Zn−Zn coordination, as confirmed by FEFF-calculated structures of

https://doi.org/10.1021/acsami.5c22636
ACS Appl. Mater. Interfaces 2026, 18, 26078−26094

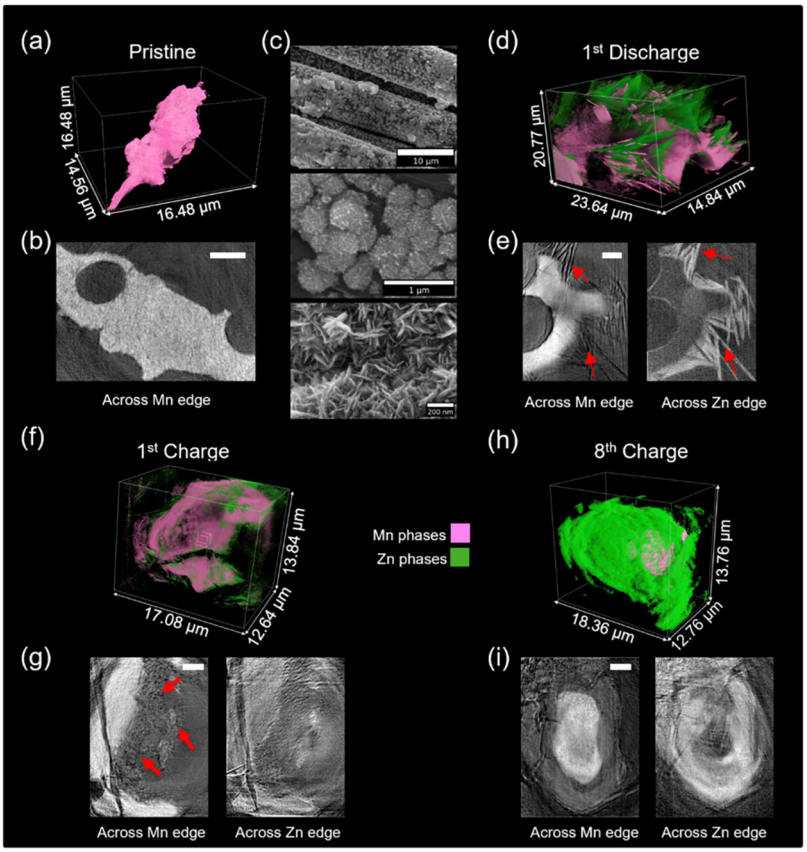

Figure 5. 3D volume rendering and 2D pseudo cross-section views from X-ray nanotomography showing the morphological evolution of the ε-MnO_2 electrode. (a, b) pristine state, (c) SEM images of the pristine state at different magnifications, (d, e) 1st discharge state (at 1 V), (f, g) 1st charge state (at 1.75 V) and (h, i) 8th cycle charge state (at 1.75 V). The scale bars in TXM images represent 10 μm.

the ZHS phase (Figure S6). At 1.6 V in the charged state, no significant peaks appear between 2−3 Å, indicating the absence of Zn−Zn coordination. However, at 1.75 V, a distinct peak emerges around 3 Å, which is comparable to the Zn−Mn coordination in the FEFF-calculated structure of $ZnMn_3O_7 \cdot 3H_2O$ (zinc−manganese complex, ZMC). To further validate these assignments, wavelet transform (WT) analysis was performed, providing complementary k−R resolution that clearly distinguishes Zn−O, Zn−Zn, and Zn−Mn scattering contributions (see Figure S7). Additionally, the WT provides complementary k−R resolution that clearly confirms the disappearance of the Zn−Zn signal (from ZHS) and the emergence of a distinct Zn−Mn scattering contribution. Since ε-MnO_2 appears to redeposit during charging, as observed in operando X-ray diffraction studies, we hypothesize that this new less crystalline phase nucleates on the surface of ZHS, forming a layered $ZnMn_3O_7 \cdot 3H_2O$ phase. This interpretation is further supported by TEM observations of the charged species, which reveal amorphous ordering alongside the redeposited ε-MnO_2 phase.[30] The absence of new diffraction peaks in our XRD data is consistent with this phase being "less crystalline" or nanostructured nature of the $ZnMn_3O_7 \cdot 3H_2O$ phase.

To further study the local chemical heterogeneity and spatial distribution of these phases, transmission X-ray microscopy (TXM) was employed.

2.3. Morphological Evolution of the ε-MnO_2 Electrode

X-rays offer high resolution and deep penetration, making them suitable for imaging fine structures and mapping chemical element distributions. Combined with tomography, X-ray microscopy provides nondestructive 3D images with nanometer-scale resolution. The morphological changes within the electrode were visualized by ex situ synchrotron X-ray nanotomography. Figure 5 presents X-ray nanotomography cross sections and 3D visualizations of the ε-MnO_2 electrode after the first and eighth cycles, across the Mn and Zn K energy absorption edges. The comparison of the two energy absorption edges enables an understanding of the morphological evolution of Mn and Zn containing phases throughout the cycling process.

A dense aggregation of the electrodeposited ε-MnO_2 particles surrounding the carbon fiber is observed across the Mn K-edge in the pristine electrode (Figure 5(a,b)). The three-dimensional architecture of the carbon cloth substrate provides increased surface area for electrodeposition and ensures strong adhesion with the active material, thereby enhancing the structural stability of the entire electrode.[55] Scanning electron microscopy (SEM) confirms a nanocrystalline structure with particle sizes in the order of a few nanometers, providing a high surface area and reduced ion diffusion pathways (Figure 5(c)) energy-dispersive X-ray spectroscopy (EDS) reveals a uniform distribution of Mn and O throughout the ε-MnO_2 electrode, with trace amounts of Zn also detected (see Figure S8). This uniform elemental distribution suggests a homogeneous composition of the electrode material.

After the initial discharge to 1 V, the electrode surface morphology changes drastically compared with the pristine

https://doi.org/10.1021/acsami.5c22636
ACS Appl. Mater. Interfaces 2026, 18, 26078−26094

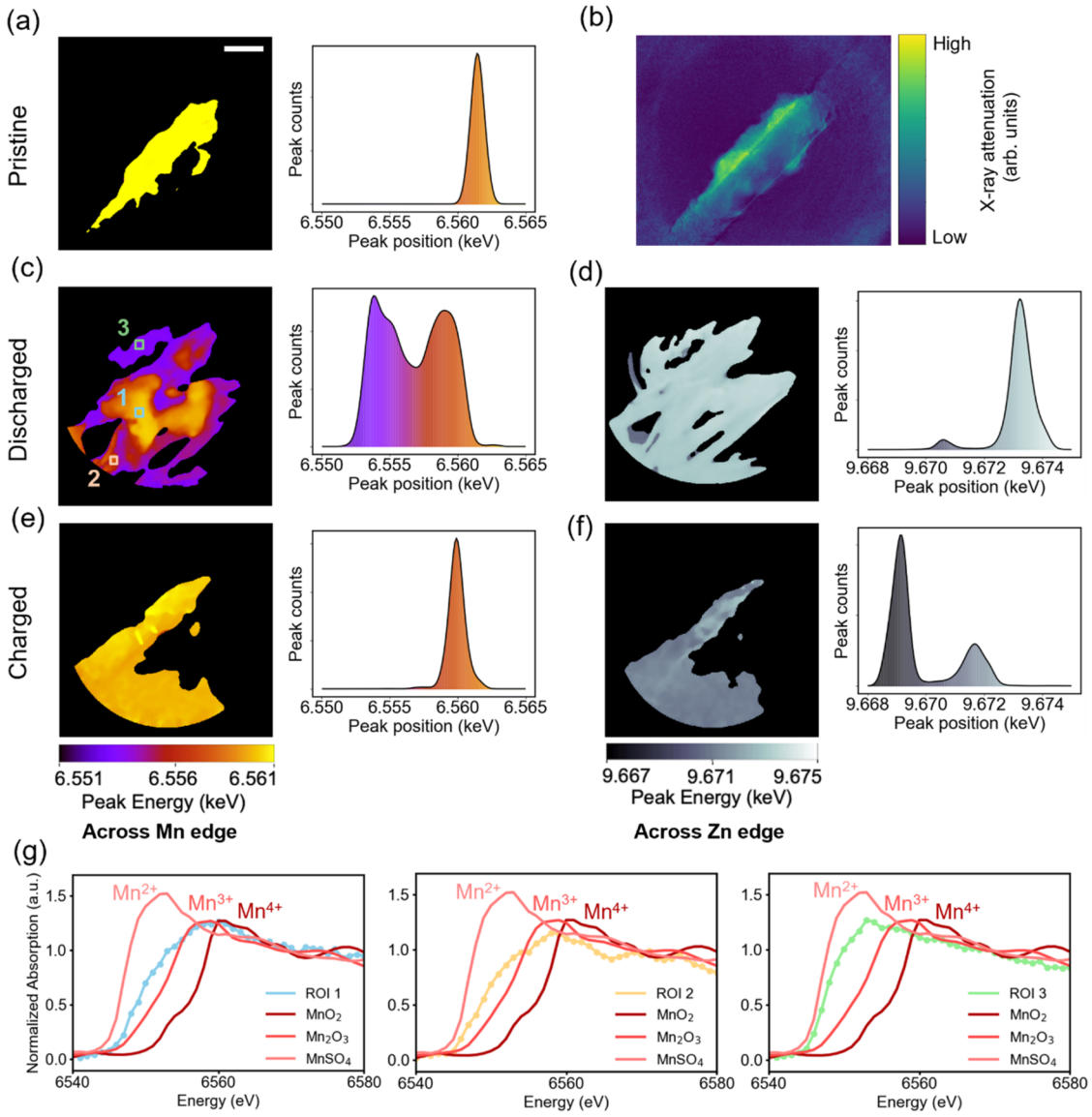

Figure 6. 2D TXM-XANES chemical map and statistical analysis. (a, b) Pristine electrode: (a) Mn K-edge chemical map and whiteline distribution, and (b) thickness profile. (c, d) First discharge: (c) Mn K-edge and (d) Zn K-edge chemical maps and distributions. (e, f) First charge: (e) Mn K-edge and (f) Zn K-edge chemical maps and distributions. (g) Mn K-edge XANES spectra from representative regions of interest (ROIs) shown in (c). The scale bar in (a) represents 10 μm.

electrode (Figure 5(d,e)). X-ray nanotomography analysis across the Mn K-edge reveals a spatial variation in MnO_2 dissolution during the initial discharge. In the outer regions (at the MnO_2-electrolyte interface), MnO_2 exhibits pronounced dissolution, which is facilitated by rapid ion diffusion and favorable kinetic conditions. However, MnO_2 particles in the regions near the carbon fiber remain undissolved, suggesting localized impedance in ion diffusion pathways and reduced reaction kinetics within this region. Across the Zn edge, formation of large flakes believed to be ZHS as seen across the outer region where MnO_2 significantly dissolved. The nucleation and growth of ZHS in the regions where MnO_2 dissolution initially occurred may impede further MnO_2 dissolution, as the formation of ZHS can create a physical barrier, effectively reducing the exposed MnO_2 surface area and limiting ion diffusion pathways necessary for continued dissolution.[56] This incomplete dissolution of MnO_2 limits the full utilization of the active material. It is important to note that the present morphological study was conducted without Mn^{2+} additives in the electrolyte. Future experiments incorporating $MnSO_4$ in the electrolyte are planned to assess its influence on spatial heterogeneity.

The first charge to 1.75 V sees the disappearance of the flaky ZHS phase and the redeposition of the dissolved Mn^{2+} on the cathode surface (Figure 5(f,g)). The low contrast image of the electrode observed across the Zn edge is likely indicative of the presence of $ZnMn_3O_7{\cdot}3H_2O$ phase along with the redeposition of the MnO_2. The disappearance of the flaky structure in the charge process confirms the reversibility of the ZHS phase. The redeposition phase appears to be predominant in regions where the ZHS phase is present, as observed during the eighth cycle charge (Figure 5(h,I)). These observations suggest that active material dissolution is hindered during discharge. Additionally, the formation of a thick, layered structure on the surface of the undissolved initial active material indicates redeposition of material onto the electrode. Figure S9 presents

https://doi.org/10.1021/acsami.5c22636
ACS Appl. Mater. Interfaces 2026, 18, 26078−26094

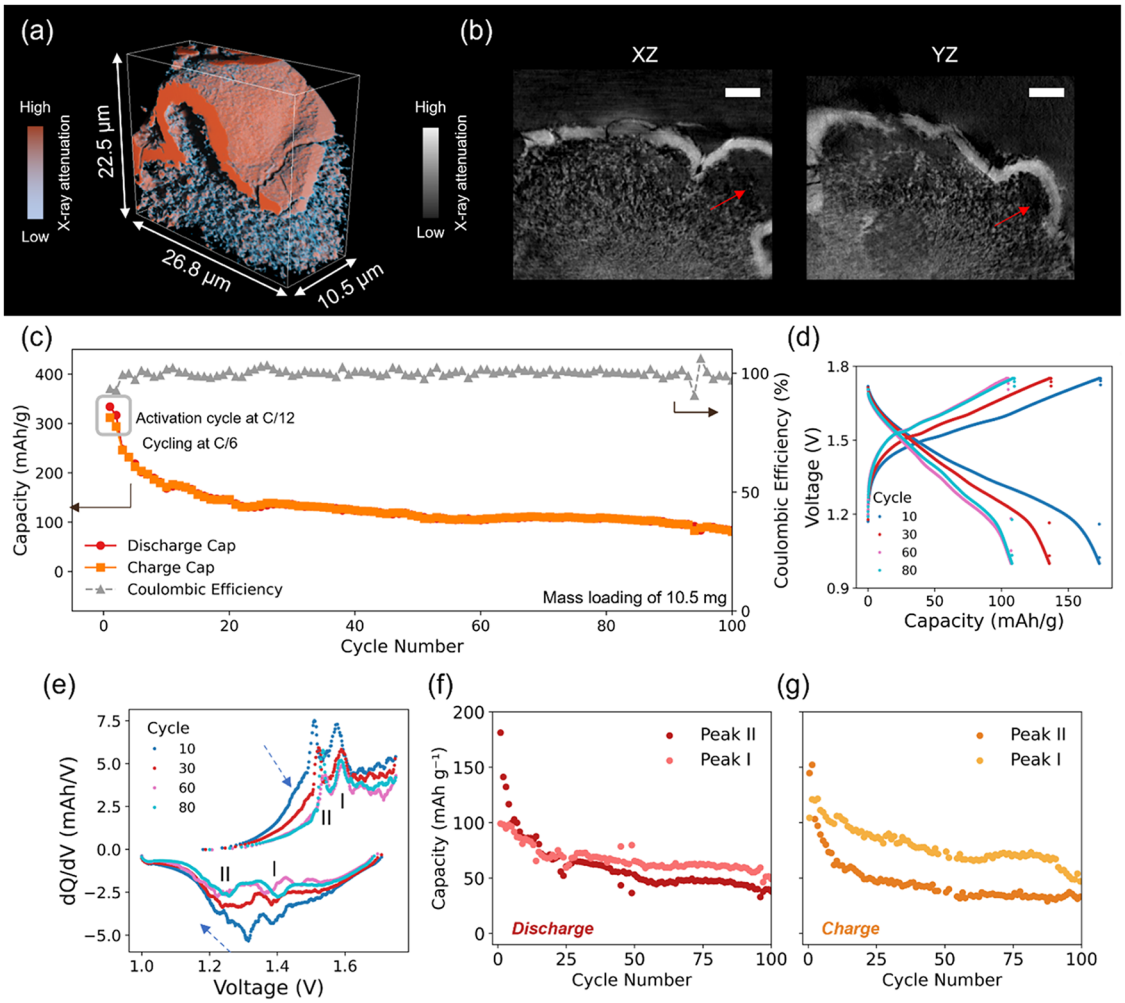

Figure 7. Morphology and electrochemical behavior of ε-MnO_2 electrode. (a) Three-dimensional morphology of the ε-MnO_2 electrode extracted after 50 cycles, characterized by transmission X-ray microscopy (TXM). (b) Corresponding two-dimensional TXM pseudo cross sections, where red arrows indicate voids due to partial dissolution of ε-MnO_2. (c–e) Electrochemical performance in 1 M $ZnSO_4$ + 0.1 M $MnSO_4$: (c) Long-term cycling stability, (d) voltage profiles, and (e) dQ/dV plots. (f, g) Integrated peak areas from dQ/dV analysis for (f) discharge and (g) charge processes.

SEM images from the post analysis of the operando XAS sample, taken at the end of the fourth charge cycle at different magnifications. Figure S9(b) highlights the formation of a layered structure on the surface of the undissolved ε-MnO_2, while images Figure S9(c,d) show higher-magnification views revealing a dense, flower-like surface morphology, which can be attributed to the $ZnMn_3O_7{\cdot}3H_2O$ phase. This distinctive morphology may facilitate Zn intercalation by providing increased surface area and favorable structural features.

The dissolution of MnO_2 and the formation of the ZHS phase during discharge play a key role in the energy-storage mechanism by creating localized regions with limited MnO_2 availability. This restricted dissolution affects the overall capacity utilization. However, the reversible formation and removal of ZHS during charging, accompanied by the redeposition of Mn^{2+}, facilitates the cycling process. The resulting surface morphology, including the formation of layered and flower-like structures, enhances the available surface area for redeposition, which directly contributes to the charge storage capacity. The morphological studies highlight the interplay between MnO_2 dissolution and Zn intercalation, with the formation of ZHS acting as a barrier that limits the dissolution of MnO_2, thereby reducing the active material's utilization. To further investigate the chemical speciation of Mn and Zn phases, XANES spectroscopy imaging was employed using transmission X-ray microscopy.

2.4. Chemical Heterogeneity of the ε-MnO_2 Electrode

To gain insight into the heterogeneity of Mn and Zn chemical phases at the micron-level after electrochemical cycling, 2D XANES spectroscopy imaging measurement was performed via TXM at the FXI (18-ID) beamline at NSLS-II. Figure 6 presents the chemical state mappings and statistical distribution of the pristine and initial cycled electrodes, identified by the white line peak positions corresponding to the maximum of the fitted curve across the X-ray absorption Mn and Zn K-edge. The statistical distribution depicts a histogram, highlighting variations in whiteline peak positions. The uniform color distribution in the pristine state 2D TXM-XANES map indicates a well-distributed MnO_2 phase and a homogeneous oxidation state in the electrodeposited ε-MnO_2 electrode (Figure 6(a)). Figure 6(b) shows the XANES profile corresponding to the thickness of the pristine electrode. In the pristine state, the Mn K-edge exhibits a uniform oxidation state, as indicated by the histogram of the white line peak

https://doi.org/10.1021/acsami.5c22636
ACS Appl. Mater. Interfaces 2026, 18, 26078−26094

position, which reveals a symmetric distribution centered at 6.561 keV.

After the initial discharge to 1 V, a heterogeneous color distribution is observed across the Mn edge, indicating an uneven reduction in the Mn valence state (Figure 6(c)). The yellow color indicates the presence of valence state closer to the pristine state, thereby confirming that some portions of the MnO_2 particles remain undissolved, which is due to the sluggish ion diffusion in the inner regions adjacent to the carbon fiber. This suggests a diffusion-limited kinetics, limiting the full utilization of the active material. The presence of Mn^{2+} and Mn^{3+}, represented by the red and purple regions in the XANES mapping, suggests the intercalation of protons or Zn^{2+} into the MnO_2 structure during the discharge process. To further examine these compositional variations, XANES spectra were extracted from representative regions in the shell and core (regions 0, 1, and 2 in Figure 6(g)). The averaged spectra reveal distinct differences in Mn oxidation states across the particle, providing qualitative evidence of compositional gradients that contribute to transport limitations and the resulting overpotential observed during discharge. Across the Zn edge, a relatively uniform color distribution is seen across the electrode surface, indicating the widespread formation of ZHS phase (Figure 6(d)). The darker regions observed in the XANES mapping, along with the subtle peak in the statistical distribution, likely correspond to the formation of Zn intercalated phase during the discharge process.

The first cycle charge sees the redeposition of the dissolved Mn^{2+}, as evidenced by the presence of a yellowish-red color in the XANES mapping across the Mn edge of the cathode surface (Figure 6(e)). However, the average oxidation states of Mn were not fully restored into that of the homogeneous pristine ε-MnO_2 after full charge, with the statistical white line peak position curve shifting to the left (Figure 6(e)). This may be attributed to diffusion limitations or the presence of newly formed Zn- and Mn-containing phases, along with the redeposition of MnO_2 during charging, which results in a lower oxidation state value. Across the Zn edge, in the charged state, the statistical white line peak position curve (Figure 6(f)) exhibits a noticeable shift toward lower energy compared to the discharged state, consistent with the bulk Zn K-edge XANES spectra shown in Figure 4(e). This shift arises from the unique interplay that contributes to the redeposition of the Mn^{2+} onto the ZHS host (Figure 6(f)). The prominent peak observed corresponds to the formation of $ZnMn_3O_7{\cdot}3H_2O$, along with the presence of a partially deintercalated phase. These findings complement recent in situ grazing-incidence XAS results, which revealed that while the bulk undergoes largely reversible insertion and extraction with Mn valence cycling between +4 and +3, the cathode-electrolyte interface experiences additional, partially irreversible processes leading to the formation of a Mn^{2+}-rich surface layer during discharge.[57] This behavior parallels our observations of chemical heterogeneity between the bulk and surface regions, suggesting that such interfacial irreversibility contributes to the observed transport limitations and early stage capacity fading.

The thickness plots and average XANES spectra for the first cycle discharge and charge states are presented in Figures S10 and S11, respectively. To further support the presence of heterogeneity across the three phases, Figure S12 shows XANES spectra from local regions of interest during the discharge and charge states.

The 3D TXM reconstruction (Figure 7(a)) reveals a core−shell morphology in the ε-MnO_2 electrode after 50 cycles, with a reconstructed surface layer approximately 2.5 μm thick. The 2D pseudo cross-sectional images (Figure 7(b)) show corresponding voids at the interface (red arrows). These features are the cumulative result of the dissolution-redeposition mechanism. During each charge, dissolved Mn^{2+} redeposits as a dense, less-crystalline Zn−Mn complex, forming the "shell." With repeated cycling, this shell thickens and passivates the electrode, leading to the electronic and ionic isolation of the underlying pristine ε-MnO_2 "core" and the formation of voids at the interface. This progressive inactivation of the original active material leads to uneven reaction fronts and is the primary contributor to the observed long-term capacity fading.

Building upon these morphological observations, to better understand the reversibility of the intercalation and dissolution processes during discharge, and the deintercalation and redeposition during charge, electrochemical potential vs capacity data was analyzed across different cycles. Differential capacity (dQ/dV) analysis was further employed to provide deeper insight into the specific contributors to the overall capacity.

2.5. Analyzing Capacity Contributions during Electrochemical Cycling

To gain insight into the reaction mechanism and stability of the Zn/ε-MnO_2 system, electrochemical cycling studies were performed. As shown in Figure 3(b), fluctuations in the concentrations of Mn and Zn species due to migration and dissolution play a key role in electrochemical behavior. To improve cycling reversibility and compensate the limited Mn in the electrolyte during operation, 0.1 M $MnSO_4$ was introduced as an electrolyte additive.

To assess performance under more practical conditions, a high mass loading cathode (10.5 mg) was employed. Given the porous architecture and three-dimensional nature of the carbon cloth performance analysis is thus discussed in terms of mass loading rather than areal capacity. The cell was initially activated with two cycles at a C-rate of C/12, followed by long-term cycling at C/6 for over 500 h (Figure 7(c)). The initial two cycles were employed to stabilize the electrochemical response of the cathode, facilitating electrode wetting and cathode-electrolyte interfacial stabilization. This slower activation rate is beneficial for mitigating the large kinetic barriers of the pristine electrode, ensuring thorough wetting of the 3D substrate. As seen in Figure 3(b), the first-cycle voltage profile differs from subsequent cycles, indicating that the primary activation processes have been completed after the second cycle. During activation, the electrode delivered a capacity exceeding 308 mAh/g, corresponding to a multielectron Mn redox process (theoretical Mn^{2+}/Mn^{4+} reaction ~616 mAh/g). A rapid drop in capacity was observed in the initial cycles, which is attributed to transport-limited capacity fade, possibly due to sluggish kinetics or loss of electroactive material.

To further investigate the evolution of electrochemical behavior, capacity vs voltage profiles were recorded at the 10th, 30th, 60th, and 80th cycles (see Figure 7(d)). These profiles revealed a continuous decline in capacity during the first 20−30 cycles, followed by stabilization at around 100 mAh/g, which was sustained over the next ~100 cycles. Corresponding differential capacity (dQ/dV) analyzes provided additional

https://doi.org/10.1021/acsami.5c22636
ACS Appl. Mater. Interfaces 2026, 18, 26078−26094

insight into the specific redox processes contributing to capacity at various stages of cycling.

When comparing the differential capacity during the activation cycle to that of the first full cycle, a major peak at ~1.3 V is observed during discharge, which corresponds to the dissolution of the active material. A corresponding reverse peak appears around 1.5 V during charging, indicating redeposition of the dissolved species (see Figure S13). This behavior is influenced by the role of ZHS as a deposition host during charge, which can reduce the activation potential required for redeposition.[50,58]

The heterogeneity observed in 2D XANES chemical maps during the first-cycle discharge and charge states (Figure S5) may contribute to reduced reversibility of the system. As shown in Figure 3(b), the Mn oxidation state changes significantly during the initial stages of discharge, suggesting that proton intercalation is the dominant process in the early phase. Based on the differential capacity analysis, we attribute the peak around 1.4 V (Peak I) to proton intercalation, and the peak at ~1.25 V (Peak II) to active material dissolution (see Figure 7(e)). During charging, the ~1.55 V peak corresponds to the reverse of dissolution, that is, Mn redeposition onto the ZHS phase (reverse of Peak II) while the ~1.6 V peak may correspond to proton deintercalation or ε-MnO_2 phase redeposition. At higher potentials, oxygen evolution or surface passivation reactions may become dominant, as suggested by the differential capacity feature above ~1.6 V, which does not correspond to a reversible redox process during discharge. These side reactions at high voltage were further investigated through chronoamperometric relaxation measurements (120 s hold at 1.75 V) performed after each charge cycle. The resulting current−time profiles for every 5 cycles (Figure S14) exhibit an initial transient decay followed by a stable residual current, consistent with the coexistence of surface passivation and parasitic oxidation processes. Although these measurements are qualitative, they support the presence of persistent side reactions that may contribute to the incomplete reoxidation of Mn at elevated potentials.

As shown in Figure 7(f,g), the quantitative evolution of the differential capacity peaks provides further evidence of these trends. The integrated intensity of Peak II (dissolution/deposition) initially decreases sharply with cycling, while Peak I (proton intercalation/deintercalation) remain relatively stable. This observation indicates that the dissolution−redeposition pathway becomes progressively less reversible, consistent with the formation of a dense surface reconstruction layer observed in the TXM analysis (Figure 7(a,b)). The growth of this shell phase can impede ion transport and confines redox activity to the outer regions of the electrode. During the initial capacity decay stage, the sharp reduction in Peak II indicates that dissolution-deposition reactions dominate the early capacity loss due to their decreasing reversibility. In contrast, during the capacity stabilization stage, Peak I associated with proton intercalation becomes the dominant contributor, highlighting a transition from surface-driven dissolution−deposition to bulk proton intercalation−controlled charge storage. Importantly, the persistence of a reduced Peak II contribution in later cycles suggests that dissolution-redeposition reactions continue but increasingly involve poorly crystalline Zn−Mn-containing phases (e.g., $ZnMn_3O_7{\cdot}3H_2O$) that are not readily detectable by X-ray diffraction. As a result, the surface-dominated dissolution-deposition reactions gradually lose reversibility, whereas proton intercalation within the remaining ε-MnO_2 lattice remains the more stable and persistent process contributing to capacity retention.

3. CONCLUSIONS

In this work, the reaction mechanism of a binder free, kinetically favorable ε-MnO_2 cathode was investigated in a mild aqueous $ZnSO_4$ electrolyte using a suite of operando synchrotron techniques. Synchrotron X-ray diffraction studies reveal a complex and competing mechanism involving proton-coupled electron transfer, proton-mediated dissolution-redeposition, and minor Zn^{2+} intercalation. This multifaceted reaction pathway was confirmed by tracking oscillations in Zn and Mn phases via X-ray absorption spectroscopy and visualizing the resulting chemical and morphological heterogeneity with 2D XANES imaging, which highlighted diffusion-limited regions of undissolved MnO_2. These studies reveal a complex mechanism involving a proton coupled electron transfer, along with a proton-mediated dissolution and redeposition, in combination with minor amount of reversible Zn^{2+} intercalation and extraction. In more practically relevant electrodes with higher mass loading, galvanostatic charge−discharge and differential capacity measurements indicate a more reversible proton intercalation process in comparison to the dissolution deposition.

To advance the development of practical Zn/MnO_2 batteries, it may be more beneficial to focus on improving reaction kinetics through controlled electrodeposition strategies or electrolyte additives that modulate water activity-rather than relying solely on pH buffer additives. Maintaining proton availability while enhancing charge transfer and structural reversibility will be key to achieving long-term performance.

Taken together, these operando results establish a unified framework for understanding ε-MnO_2 charge storage. Proton-coupled electron transfer, proton-mediated dissolution-redeposition, and minor Zn^{2+} intercalation is shown to coexist and compete during cycling, giving rise to spatial and chemical heterogeneity within the cathode. These insights provide design guidance for future Zn/MnO_2 systems, where controlling proton transport, water activity, and electrode morphology will be critical for improving reversibility and long-term stability.

4. EXPERIMENTAL SECTION

4.1. Electrode Preparation and Electrodeposition of ε-MnO_2

A ratio of 1 mg of multiwalled carbon nanotubes (MWCNTs) to 2 mL of isopropyl alcohol was used to prepare the dispersion, which was then sonicated for 2 h. The suspension was filtered through an electrophilic carbon cloth (Fuel Cell Store) with filter paper, using vacuum filtration. The MWCNT coated carbon cloth was activated in 67% nitric acid solution for 24 h to improve its hydrophilicity. After washing and the electrode was dried in a vacuum oven at 60 °C for 2 h. The active material to carbon additive ratio was maintained at 85:15. The ε-MnO_2 electrodes were synthesized by electrodeposition via a two-electrode cell with the MWCNT coated carbon cloth as the working electrode, Zn metal foil as both counter and reference electrodes in a 1 M $ZnSO_4$ + 0.5 M $MnSO_4$ + 0.1 M H_2SO_4 aqueous solution. Galvanostatic charge was applied on the cell at 1 mA cm^{-2} to 2.2 V (vs Zn/Zn^{2+}) for a stipulated time depending upon the required capacity. The ε-MnO_2 electrode was rinsed thoroughly with distilled water and dried overnight in a vacuum oven at 60 °C.

https://doi.org/10.1021/acsami.5c22636
ACS Appl. Mater. Interfaces 2026, 18, 26078−26094

4.2. Cell Assembly and Electrochemical Characterization

Standard coin cells were assembled using Glass fiber (Whatman) as the separator between the ε-MnO_2 cathode and zinc anode (100 μm in thickness). The electrolyte used was 1 M $ZnSO_4$ + 0.1 M $MnSO_4$ and 100 μL was added in each cell. Charge and discharge electrochemical tests were conducted using a Biologic VSP300 potentiostat with a voltage range of 1−1.75 V. The C-rates were defined by estimating the deposited mass of MnO_2 and experimental capacity of 300 mA h $g_{MnO_2}^{-1}$, based on electrochemical testing. Differential capacity (dQ/dV) analysis was performed by calculating finite differences of charge (Q) and voltage (V) data. The resulting curves were smoothed using a Savitzky−Golay filter to reduce noise. For the area quantifications, a cutoff point was defined at the local maximum between the two discharge peaks and the local minimum between the charge peaks. The integrated areas on either side of these cutoff points were then used to estimate the relative contributions of the dissolution−deposition and intercalation processes. Chronoamperometric relaxation measurements were conducted after each charge cycle. The cell potential was held at 1.75 V for 120 s measured every 10 s, and the resulting current decay was recorded. The transient current response reflects relaxation processes associated with surface redox reactions and parasitic charge transfer, providing insight into the reversibility of the electrode−electrolyte interface during cycling. Postcycled scanning electron microscopy and energy dispersive spectroscopy maps were carried out on the electrodes with JEOL 7600 SEM at a bias of 15 keV at the Center for Functional Nanomaterials (CFN), Brookhaven National Laboratory (BNL). The pH of the electrolytes was measured at room temperature using an Orion STAR A211 pH meter.

4.3. X-ray Photoelectron Spectroscopy

X-ray photoelectron spectroscopy (XPS) measurements were collected on washed and dried ε-MnO_2 cathodes. The measurements were conducted at the Center for Functional Nanomaterials (CFN) at Brookhaven National Laboratory (BNL) under a base pressure of 2×10^{-7} Pa in an ultrahigh vacuum chamber. A nonmonochromatized Al Kα X-ray source ($h\nu$ = 1486.6 eV, 15 kV, 20 mA) and a SPECS Phoibos 100 MCD analyzer were used as the X-ray source and detector, respectively.

An energy pass (E_{pass}) of 20 eV and a step size of 0.05 eV were used for the C 1s, O 1s, Mn 2p, and Zn 2p spectral regions, while a finer step size of 0.02 eV was used for the Mn 3s region.

All XPS spectra were fitted using CasaXPS software.[59] A Shirley background was applied, and the peak shapes were modeled using a Gaussian−Lorentzian line shape. Equation 7 was used to calculate the relative surface concentrations (X_i) of the detected components.

$$X_i = \frac{\frac{A_i}{S_i}}{\sum_{i=1}^{n} \frac{A_i}{S_i}} \tag{7}$$

Where A_i is the area of each fitted component, and S_i is the sensitivity factor for the corresponding element, including instrumental correction factors.

The AOS was estimated to be 3.5 for a ΔBE of 4.82 eV (see Figure S15). The XPS analysis also revealed the presence of some Zn^{2+} cations, originating from the metal oxide lattice, as the electrodes were rinsed with Milli-Q water prior to analysis to eliminate any contribution from the electrolyte.

4.4. Synchrotron Characterization and Data Analysis

4.4.1. Synchrotron Operando X-ray Diffraction Studies of Crystalline Phase Evolution. *4.4.1.1. Operando XRD Setup.* The X-ray diffraction experiments were conducted at the X-ray powder diffraction beamline (XPD, 28-ID-2) at NSLS-II, BNL. A 2D amorphous-silicon digital X-ray detector with 2048 × 2048 pixels, pixel size 200 × 200 μm^2 was utilized to collect the diffraction rings in transmission mode. The X-ray beam size was 0.5 mm × 0.5 mm. The diffraction rings in each 2D image were azimuthally integrated and reduced to an intensity vs 2θ (diffraction angle) plot via a Python-based program DIOPTAS.[60] To identify the corresponding phases, the peak profiles were first compared with the standard references provided by a commercial database including JADE and PDF-4+ 2020 (JCPDS-ICDD).

4.4.1.2. Cell Configuration and Data Acquisition. Operando X-ray diffraction was performed in a modified coin-cell with a 3 mm observation window opened on the casing, spacer and Zn anode sealed with Kapton film and epoxy. Multiple cells were cycled simultaneously between 1.0−1.75 V with varying electrolyte concentrations. Data was collected at 67.18 keV (λ = 0.1811 Å); the sample−detector distance was calibrated using a CeO_2 standard. Each 2D pattern used a 30 s exposure. Two experiments were conducted: the first (1 M $ZnSO_4$ in H_2O) collected scans approximately every 8 min, and the second (1 M $ZnSO_4$ in H_2O vs D_2O comparison) was recorded continuously with ∼4 min intervals between scans.

4.4.1.3. Rietveld Refinement and Model Parameters. Sequential time-series refinements were performed using TOPAS-Academic (Coelho Software, v6). Lattice parameters, phase fractions, and Zn occupancy were refined as a function of cycling state using ε-MnO_2 (PDF Card #04−005−4883), carbon (PDF Card #04−015−2407), and $Zn_4SO_4(OH)_6{\cdot}5H_2O$ (ZHS, PDF Card #04−012−8189) phases. The ZHS phase was introduced only after its corresponding diffraction peaks appeared. Zn occupancy at the Mn site was allowed to vary between 0 and 0.5. Backgrounds were modeled with a 12-term Chebyshev polynomial. A fourth-order spherical-harmonics preferred-orientation correction was applied to MnO_2. Instrumental and sample broadening were modeled using pseudo-Voigt-type profiles with θ-dependent Gaussian and Lorentzian FWHM terms [$\tan(\theta)$ and $1/\cos(\theta)$], along with Lorentzian size and strain terms. Axial divergence and polarization were modeled with a simple axial model and Lorentz factor.

4.4.1.4. Normalization and Uncertainty Analysis. Phase scale factors were refined for each scan. Weight fractions were normalized to the electrochemically inactive carbon phase to mitigate effects of changing illuminated volume, absorption, or beam fluctuations. Parameter uncertainties (including phase fractions and Zn occupancy) were estimated as one-sigma standard deviations derived from the least-squares covariance matrix and propagated to derived quantities. The parameter-correlation matrix was inspected to prevent overparameterization. In the figures, shaded regions or line thicknesses indicate the corresponding uncertainty ranges.

4.4.1.5. Synchrotron Operando and Ex Situ X-ray Absorption Spectroscopic Studies on Chemical Evolution. The operando X-ray absorption spectroscopy (XAS) experiment was conducted at the quick X-ray absorption and scattering (QAS) beamline (7-BM) at the NSLS-II, BNL. The Mn and Zn K-edge absorption spectra were acquired using a channel-cut Si(111) crystal monochromator in continuous scan mode. Spectra were recorded from the cathode in transmission and fluorescence mode, with scanning and data acquisition times of approximately 30 s per spectrum.

The ex situ Zn XAS experiment was performed at the inner shell spectroscopy (ISS) beamline (8-ID) at NSLS-II, BNL. For the ex situ data, 20 spectra were collected at the Zn K-edge to ensure an adequate signal-to-noise ratio.

For the operando XAS experiments, a custom-built cell was used with the cathode and anode positioned in the same plane. Five spectra were collected at the Mn K-edge and five at the Zn K-edge; spectra from each time point were averaged to achieve an adequate signal-to-noise ratio. The Larch analysis package was used to batch process the operando spectra.[61] This process included averaging the spectra and extracting data at specific time points. The Mn and Zn edge jump was quantified by linear regression fits to the pre-edge (6350−6570 eV) and postedge (6880−7400 eV) regions of the merged spectra, followed by interpolation at the peak of the first derivative. The X-ray absorption edge and quantifications of the edge jump is presented in Figure S16.

To study the oxidation state of the operando data set, the edge was first calibrated using the integral method using integration limits of 6548−6556 eV for Mn. To accurately determine the edge energy from

https://doi.org/10.1021/acsami.5c22636
ACS Appl. Mater. Interfaces 2026, 18, 26078−26094

the X-ray absorption spectra, the edge integral method was employed.[53,54] For Mn, this integration method was used to calculate the edge position, as it provides a linear relationship between the edge position and the Mn oxidation state within acceptable residual limits (Figure S17).

The EXAFS spectra were Fourier-transformed into *R*-space and qualitatively compared using Athena, with theoretical scattering paths calculated by FEFF6 based on reference crystal structures of $Zn_4SO_4(OH)_6{\cdot}5H_2O$ (ZHS) and $ZnMn_3O_7{\cdot}3H_2O$. The analysis was aimed at identifying changes in Zn−O, Zn−Zn, and Zn−Mn coordination environments. For consistency, each EXAFS region was analyzed within a k-range of 2−10 $Å^{-1}$ using a Hanning window (dk = 2), and an *R*-range of 1.0−3 Å was applied across all samples. In addition, wavelet transform (WT) analysis was performed using the Cauchy wavelet function implemented in Larch python package to provide joint k−R resolution and further confirm the Zn−O, Zn−Zn, and Zn−Mn coordination features observed in *R*-space.[61]

4.4.1.6. Synchrotron X-ray Nanotomography to Study Morphological Evolution. The synchrotron X-ray nanotomography and spectroscopic imaging experiment was carried out through transmission X-ray microscopy (TXM) at the Full-field X-ray Imaging beamline (FXI, 18-ID) at NSLS-II, BNL. The images from the TXM at FXI were captured by a lens-coupled charge-coupled device detector (2560 × 2160 pixels), providing a 46.8 × 55.48 μm^2 (horizontal × vertical) field of view, under a camera binning of 2 × 2 and magnification of ×300 with an effective pixel size of 43.34 nm. The cycled electrodes were cut into a wedge shape with a tip size less than 50 μm and mounted onto stainless steel pins using epoxy. The X-ray incident energy used was 7.0 and 6.5 keV corresponding to above and below the Mn K-edge (6.539 keV), while 9.7 and 9.5 keV were chosen for the above and below Zn K-edge (9.659 keV), ensuring optimal imaging contrast for the Mn and Zn complex phases. Over 850 projections were collected per tomography with an exposure time of 50−100 ms per projection image and total acquisition time of 1−1.5 min per scan. Following image acquisition, tomographic reconstruction was conducted with the Gridrec algorithm using the python package Tomopy.[62,63]

4.4.2. XANES Imaging Analysis. The electrodes were extracted from coin cells at the desired electrochemical states, then immediately rinsed with deionized water and dried under vacuum at 60 °C overnight to remove residual electrolyte species prior to XANES mapping.

For chemical state mapping, a series of 2D TXM images were collected as a function of incident X-ray energy across the Mn and Zn K-edge using 101 energy points (from 6.41−6.98 keV) and 86 energy points (from 9.53−9.71 keV) respectively. The energy of the XANES images were calibrated with a Zn and Mn metal foils and aligned to the Zn and Mn K-edge. The 2D XANES data was processed using pyXAS package (an open-source package for 2D XANES analysis).[64] A camera binning of 4 × 4 was used, resulting in an effective pixel size of 86.68 nm. Alignment of the images collected at different energy points was done using a built-in StackReg method. A physics informed machine learning model was implemented to improve the signal-to-noise ratio of the XANES image. A pre-edge normalization using a second-degree polynomial was used to fit the pre-edge. K-means clustering masks were generated to filter out the nonactive components in the image. Athena software package was used to normalize, calibrate the XANES data, and confirm the oxidation states of Mn and Zn in each sample.[65] The chemical state of each pixel was determined by spline curve fitting of the white-line energy positions from the spectroscopic images.

■ ASSOCIATED CONTENT

Supporting Information

The Supporting Information is available free of charge at https://pubs.acs.org/doi/10.1021/acsami.5c22636.

Electrochemical and transport analysis of interfacial pH evolution; Mn−H_2O Pourbaix diagram, voltage−time profile of ε-MnO_2 electrodeposition; operando X-ray diffraction and Rietveld refinement of pristine, discharged, and charged states; unit-cell volume evolution during cycling; crystallographic structure of ε-MnO_2; operando Mn K-edge XANES and EXAFS analysis; FEFF-calculated local structures of ZHS and $ZnMn_3O_7{\cdot}3H_2O$; wavelet transform analysis of Zn K-edge EXAFS; SEM and EDX elemental mapping; transmission X-ray microscopy (TXM) XANES thickness profiles; spatially resolved XANES heterogeneity; electrochemical profiles and differential capacity analysis for high mass-loading electrodes; chronoamperometric relaxation behavior; XPS analysis of pristine ε-MnO_2; XANES edge determination and normalization; and calibration of Mn oxidation states using reference compounds (PDF)

■ AUTHOR INFORMATION

Corresponding Author

Yu-chen Karen Chen-Wiegart − *Department of Materials Science and Chemical Engineering, Stony Brook University, Stony Brook, New York 11794, United States; National Synchrotron Light Source II, Brookhaven National Laboratory, Upton, New York 11973, United States;* orcid.org/0000-0003-4445-2159; Email: Karen.Chen-Wiegart@stonybrook.edu

Authors

Varun R. Kankanallu − *Department of Materials Science and Chemical Engineering, Stony Brook University, Stony Brook, New York 11794, United States;* orcid.org/0000-0002-0954-5803

Adesanmi Adeniyi − *Department of Materials Science and Chemical Engineering, Stony Brook University, Stony Brook, New York 11794, United States*

Jianming Bai − *National Synchrotron Light Source II, Brookhaven National Laboratory, Upton, New York 11973, United States;* orcid.org/0000-0002-0575-2987

Lu Ma − *National Synchrotron Light Source II, Brookhaven National Laboratory, Upton, New York 11973, United States*

Hui Zhong − *National Synchrotron Light Source II, Brookhaven National Laboratory, Upton, New York 11973, United States*

Xianghui Xiao − *National Synchrotron Light Source II, Brookhaven National Laboratory, Upton, New York 11973, United States;* orcid.org/0000-0002-7142-3452

Zhongshu Ren − *National Synchrotron Light Source II, Brookhaven National Laboratory, Upton, New York 11973, United States*

Steven Ehrlich − *National Synchrotron Light Source II, Brookhaven National Laboratory, Upton, New York 11973, United States*

Jorge Moncada − *National Synchrotron Light Source II, Brookhaven National Laboratory, Upton, New York 11973, United States*

Akhil Tayal − *National Synchrotron Light Source II, Brookhaven National Laboratory, Upton, New York 11973, United States;* orcid.org/0000-0001-8152-4209

Eli Stavitski − *National Synchrotron Light Source II, Brookhaven National Laboratory, Upton, New York 11973, United States;* orcid.org/0000-0002-3337-2930

Xiao Tong − *Center for Functional Nanomaterials, Brookhaven National Laboratory, Upton, New York 11973, United States*

Kenneth J. Takeuchi − *Department of Materials Science and Chemical Engineering, Stony Brook University, Stony Brook, New York 11794, United States; Energy and Photon Sciences Directorate, Brookhaven National Laboratory, Upton, New York 11973, United States; Department of Chemistry and Institute of Sustainability, Electrification, and Energy (I:SEE), Stony Brook University, Stony Brook, New York 11794, United States;* orcid.org/0000-0001-8129-444X

Amy C. Marschilok − *Department of Materials Science and Chemical Engineering, Stony Brook University, Stony Brook, New York 11794, United States; Energy and Photon Sciences Directorate, Brookhaven National Laboratory, Upton, New York 11973, United States; Department of Chemistry and Institute of Sustainability, Electrification, and Energy (I:SEE), Stony Brook University, Stony Brook, New York 11794, United States;* orcid.org/0000-0001-9174-0474

Esther S. Takeuchi − *Department of Materials Science and Chemical Engineering, Stony Brook University, Stony Brook, New York 11794, United States; Energy and Photon Sciences Directorate, Brookhaven National Laboratory, Upton, New York 11973, United States; Department of Chemistry and Institute of Sustainability, Electrification, and Energy (I:SEE), Stony Brook University, Stony Brook, New York 11794, United States;* orcid.org/0000-0001-8518-1047

Mingyuan Ge − *National Synchrotron Light Source II, Brookhaven National Laboratory, Upton, New York 11973, United States;* orcid.org/0000-0001-5682-7443

Complete contact information is available at: https://pubs.acs.org/10.1021/acsami.5c22636

Notes

The authors declare no competing financial interest.

■ ACKNOWLEDGMENTS

This research was supported by the Center for Mesoscale Transport Properties, an Energy Frontier Research Center supported by the U.S. Department of Energy, Office of Science, Basic Energy Sciences, under award #DE-SC0012673. This research used resources, X-ray Powder Diffraction beamline (XPD, 28-ID-2), Quick X-ray Absorption and Scattering (QAS, 7-BM), Inner-Shell Spectroscopy (ISS, 8-ID) and Full Field X-ray Imaging beamline (FXI, 18-ID) of the National Synchrotron Light Source II, a U.S. Department of Energy (DOE) Office of Science by Brookhaven National Laboratory under Contract No. DE-SC0012704. This research used Materials Synthesis and Characterization Facility of the Center for Functional Nanomaterials (CFN), which is a U.S. Department of Energy Office of Science User Facility, at Brookhaven National Laboratory under Contract No. DE-SC0012704. We thank Dr. Sanjit Ghose for his leadership of the XPD team - the development of beamline capabilities used in this work, user support, and collaborative efforts. We thank the support of Data Science and System Integration staff, Steven LaMarra and XPD beamline staff, John Trunk for support in setting up operando experiment. EST acknowledges the support of the William and Jane Knapp Chair of Energy and the Environment.

■ REFERENCES

(1) Liu, H.; Wang, J.-G.; You, Z.; Wei, C.; Kang, F.; Wei, B. Rechargeable aqueous zinc-ion batteries: Mechanism, design strategies and future perspectives. *Mater. Today* **2021**, *42*, 73−98.

(2) Fang, G.; Zhou, J.; Pan, A.; Liang, S. Recent Advances in Aqueous Zinc-Ion Batteries. *ACS Energy Lett.* **2018**, *3* (10), 2480−2501.

(3) Zhou, T.; Zhu, L.; Xie, L.; Han, Q.; Yang, X.; Chen, L.; Wang, G.; Cao, X. Cathode materials for aqueous zinc-ion batteries: A mini review. *J. Colloid Interface Sci.* **2022**, *605*, 828−850.

(4) Xu, C.; Li, B.; Du, H.; Kang, F. Energetic Zinc Ion Chemistry: The Rechargeable Zinc Ion Battery. *Angew. Chem., Int. Ed.* **2012**, *51* (4), 933−935.

(5) Mallick, S.; Raj, C. R. Aqueous Rechargeable Zn-ion Batteries: Strategies for Improving the Energy Storage Performance. *ChemSusChem* **2021**, *14* (9), 1987−2022.

(6) Bag, S.; Thakur, V. S.; Bhadra, A.; Banerjee, S.; Kundu, D.; Raj, C. R. Vacancy-Engineered Vanadium Cathode for Fast-Charging Aqueous Zinc Batteries of Ultra-Long Cycle Life. *Adv. Funct. Mater.* **2026**, *36*, No. e15788.

(7) Mallick, S.; Choutipalli, V. S. K.; Bag, S.; Subramanian, V.; Raj, C. R. Defect Engineered Ternary Spinel: An Efficient Cathode for an Aqueous Rechargeable Zinc-Ion Battery of Long-Term Cyclability. *ACS Appl. Mater. Interfaces* **2022**, *14* (33), 37577−37586.

(8) Li, G.; Sun, L.; Zhang, S.; Zhang, C.; Jin, H.; Davey, K.; Liang, G.; Liu, S.; Mao, J.; Guo, Z. Developing Cathode Materials for Aqueous Zinc Ion Batteries: Challenges and Practical Prospects. *Adv. Funct. Mater.* **2024**, *34* (5), No. 2301291.

(9) Kundu, D.; Adams, B. D.; Duffort, V.; Vajargah, S. H.; Nazar, L. F. A high-capacity and long-life aqueous rechargeable zinc battery using a metal oxide intercalation cathode. *Nat. Energy* **2016**, *1* (10), No. 16119.

(10) Liu, Z.; Pulletikurthi, G.; Endres, F. A Prussian Blue/Zinc Secondary Battery with a Bio-Ionic Liquid−Water Mixture as Electrolyte. *ACS Appl. Mater. Interfaces* **2016**, *8* (19), 12158−12164.

(11) Häupler, B.; Rössel, C.; Schwenke, A. M.; Winsberg, J.; Schmidt, D.; Wild, A.; Schubert, U. S. Aqueous zinc-organic polymer battery with a high rate performance and long lifetime. *NPG Asia Mater.* **2016**, *8* (7), e283.

(12) Zhang, N.; Chen, X.; Yu, M.; Niu, Z.; Cheng, F.; Chen, J. Materials chemistry for rechargeable zinc-ion batteries. *Chem. Soc. Rev.* **2020**, *49* (13), 4203−4219.

(13) Xue, T.; Fan, H. J. From aqueous Zn-ion battery to Zn-MnO2 flow battery: A brief story. *J. Energy Chem.* **2021**, *54*, 194−201.

(14) Pan, H.; Shao, Y.; Yan, P.; Cheng, Y.; Han, K. S.; Nie, Z.; Wang, C.; Yang, J.; Li, X.; Bhattacharya, P.; et al. Reversible Aqueous Zinc/Manganese Oxide Energy Storage from Conversion Reactions. *Nat. Energy* **2016**, *1*, No. 16039.

(15) Biswal, A.; Tripathy, B. C.; Sanjay, K.; Subbaiah, T.; Minakshi, M. Electrolytic manganese dioxide (EMD): a perspective on worldwide production, reserves and its role in electrochemistry. *RSC Adv.* **2015**, *5* (72), 58255−58283.

(16) Wang, F.; Zheng, Y.; Chen, Q.; Yan, Z.; Lan, D.; Lester, E.; Wu, T. A critical review of facets and defects in different MnO2 crystalline phases and controlled synthesis − Its properties and applications in the energy field. *Coord. Chem. Rev.* **2024**, *500*, No. 215537.

(17) Ghosh, S. K. Diversity in the Family of Manganese Oxides at the Nanoscale: From Fundamentals to Applications. *ACS Omega* **2020**, *5* (40), 25493−25504.

(18) Alfaruqi, M. H.; Gim, J.; Kim, S.; Song, J.; Jo, J.; Kim, S.; Mathew, V.; Kim, J. Enhanced reversible divalent zinc storage in a structurally stable α-MnO2 nanorod electrode. *J. Power Sources* **2015**, *288*, 320−327.

(19) Han, M.; Huang, J.; Liang, S.; Shan, L.; Xie, X.; Yi, Z.; Wang, Y.; Guo, S.; Zhou, J. Oxygen Defects in β-MnO2 Enabling High-Performance Rechargeable Aqueous Zinc/Manganese Dioxide Battery. *iScience* **2020**, *23* (1), No. 100797.

(20) Alfaruqi, M. H.; Mathew, V.; Gim, J.; Kim, S.; Song, J.; Baboo, J. P.; Choi, S. H.; Kim, J. Electrochemically Induced Structural

Transformation in a γ-MnO2 Cathode of a High Capacity Zinc-Ion Battery System. *Chem. Mater.* **2015**, *27*, 3609−3620.
(21) Wang, C.; Zeng, Y.; Xiao, X.; Wu, S.; Zhong, G.; Xu, K.; Wei, Z.; Su, W.; Lu, X. γ-MnO2 nanorods/graphene composite as efficient cathode for advanced rechargeable aqueous zinc-ion battery. *J. Energy Chem.* **2020**, *43*, 182−187.
(22) Alfaruqi, M. H.; Gim, J.; Kim, S.; Song, J.; Pham, D. T.; Jo, J.; Xiu, Z.; Mathew, V.; Kim, J. A layered δ-MnO2 nanoflake cathode with high zinc-storage capacities for eco-friendly battery applications. *Electrochem. Commun.* **2015**, *60*, 121−125.
(23) Wang, L.; Cao, X.; Xu, L.; Chen, J.; Zheng, J. Transformed Akhtenskite MnO2 from Mn3O4 as Cathode for a Rechargeable Aqueous Zinc Ion Battery. *ACS Sustainable Chem. Eng.* **2018**, *6* (12), 16055−16063.
(24) Wu, X.; Xiang, Y.; Peng, Q.; Wu, X.; Li, Y.; Tang, F.; Song, R.; Liu, Z.; He, Z.; Wu, X. Green-low-cost rechargeable aqueous zinc-ion batteries using hollow porous spinel ZnMn2O4 as the cathode material. *J. Mater. Chem. A* **2017**, *5* (34), 17990−17997.
(25) Kim, C.-H.; Akase, Z.; Zhang, L.; Heuer, A. H.; Newman, A. E.; Hughes, P. J. The structure and ordering of ε-MnO2. *J. Solid State Chem.* **2006**, *179* (3), 753−774.
(26) Li, L.; Hoang, T. K. A.; Zhi, J.; Han, M.; Li, S.; Chen, P. Functioning Mechanism of the Secondary Aqueous Zn-β-MnO2 Battery. *ACS Appl. Mater. Interfaces* **2020**, *12* (11), 12834−12846.
(27) Kankanallu, V. R.; Zheng, X.; Leschev, D.; Zmich, N.; Clark, C.; Lin, C.-H.; Zhong, H.; Ghose, S.; Kiss, A. M.; Nykypanchuk, D.; et al. Elucidating a dissolution−deposition reaction mechanism by multimodal synchrotron X-ray characterization in aqueous Zn/MnO2 batteries. *Energy Environ. Sci.* **2023**, *16* (6), 2464−2482.
(28) Gao, X.; Wu, H.; Li, W.; Tian, Y.; Zhang, Y.; Wu, H.; Yang, L.; Zou, G.; Hou, H.; Ji, X. H+-Insertion Boosted α-MnO2 for an Aqueous Zn-Ion Battery. *Small* **2020**, *16* (5), No. 1905842.
(29) Yuan, Y.; Sharpe, R.; He, K.; Li, C.; Saray, M. T.; Liu, T.; Yao, W.; Cheng, M.; Jin, H.; Wang, S.; et al. Understanding intercalation chemistry for sustainable aqueous zinc−manganese dioxide batteries. *Nat. Sustainability* **2022**, *5* (10), 890−898.
(30) Aguilar, I.; Lemaire, P.; Ayouni, N.; Bendadesse, E.; Morozov, A. V.; Sel, O.; Balland, V.; Limoges, B.; Abakumov, A. M.; Raymundo-Piñero, E.; et al. Identifying interfacial mechanisms limitations within aqueous Zn-MnO2 batteries and means to cure them with additives. *Energy Storage Mater.* **2022**, *53*, 238−253.
(31) Xiao, X.; Zhang, Z.; Wu, Y.; Xu, J.; Gao, X.; Xu, R.; Huang, W.; Ye, Y.; Oyakhire, S. T.; Zhang, P.; et al. Ultrahigh-Loading Manganese-Based Electrodes for Aqueous Batteries via Polymorph Tuning. *Adv. Mater.* **2023**, *35* (33), No. 2211555.
(32) Sun, W.; Wang, F.; Hou, S.; Yang, C.; Fan, X.; Ma, Z.; Gao, T.; Han, F.; Hu, R.; Zhu, M.; Wang, C. Zn/MnO2 Battery Chemistry With H+ and Zn2+ Coinsertion. *J. Am. Chem. Soc.* **2017**, *139* (29), 9775−9778.
(33) Kozawa, A.; Yeager, J. F. The Cathodic Reduction Mechanism of Electrolytic Manganese Dioxide in Alkaline Electrolyte. *J. Electrochem. Soc.* **1965**, *112* (10), 959−963.
(34) Chabre, Y.; Pannetier, J. Structural and electrochemical properties of the proton/γ-MnO2 system. *Prog. Solid State Chem.* **1995**, *23*, 1−130.
(35) Black, A. P.; Sorrentino, A.; Fauth, F.; Yousef, I.; Simonelli, L.; Frontera, C.; Ponrouch, A.; Tonti, D.; Palacín, M. R. Synchrotron radiation based operando characterization of battery materials. *Chem. Sci.* **2023**, *14* (7), 1641−1665.
(36) Wang, L.; Wang, J.; Zuo, P. Probing Battery Electrochemistry with In Operando Synchrotron X-Ray Imaging Techniques. *Small Methods* **2018**, *2* (8), No. 1700293.
(37) Gallaway, J. W.; Gaikwad, A. M.; Hertzberg, B.; Erdonmez, C. K.; Chen-Wiegart, Y.-c. K.; Sviridov, L. A.; Evans-Lutterodt, K.; Wang, J.; Banerjee, S.; Steingart, D. A. An In Situ Synchrotron Study of Zinc Anode Planarization by a Bismuth Additive. *J. Electrochem. Soc.* **2014**, *161* (3), A275−A284.
(38) Tang, F.; Wu, Z.; Yang, C.; Osenberg, M.; Hilger, A.; Dong, K.; Markötter, H.; Manke, I.; Sun, F.; Chen, L.; Cui, G. Synchrotron X-Ray Tomography for Rechargeable Battery Research: Fundamentals, Setups and Applications. *Small Methods* **2021**, *5* (9), No. 2100557.
(39) Chu, Y. S.; Lee, W.-K.; Tappero, R.; Ge, M.; Huang, X.; Xiao, X.; Yan, H.; Northrup, P.; Thieme, J.; Kiss, A. M.; et al. Multimodal, Multidimensional, and Multiscale X-ray Imaging at the National Synchrotron Light Source II. *Synchrotron Radiation News* **2020**, *33* (3), 29−36.
(40) Chen-Wiegart, Y.-C. K.; Waluyo, I.; Kiss, A.; Campbell, S.; Yang, L.; Dooryhee, E.; Trelewicz, J. R.; Li, Y.; Gates, B.; Rivers, M.; Yager, K. G. Multimodal Synchrotron Approach: Research Needs and Scientific Vision. *Synchrotron Radiation News* **2020**, *33* (1), 44−47.
(41) Clarke, C. J.; Browning, G. J.; Donne, S. W. An RDE and RRDE Study into the Electrodeposition of Manganese Dioxide. *Electrochim. Acta* **2006**, *51*, 5773−5784.
(42) Kao, W. H.; Weibel, V. J. Electrochemical oxidation of manganese(II) at a platinum electrode. *J. Appl. Electrochem.* **1992**, *22* (1), 21−27.
(43) Chao, D.; Zhou, W.; Ye, C.; Zhang, Q.; Chen, Y.; Gu, L.; Davey, K.; Qiao, S.-Z. An Electrolytic Zn−MnO2 Battery for High-Voltage and Scalable Energy Storage. *Angew. Chem., Int. Ed.* **2019**, *58* (23), 7823−7828.
(44) Galakhov, V. R.; Demeter, M.; Bartkowski, S.; Neumann, M.; Ovechkina, N. A.; Kurmaev, E. Z.; Lobachevskaya, N. I.; Mukovskii, Y. M.; Mitchell, J.; Ederer, D. L. Mn3s exchange splitting in mixed-valence manganites. *Phys. Rev. B* **2002**, *65* (11), No. 113102.
(45) Ruetschi, P. Cation-Vacancy Model for MnO2. *J. Electrochem. Soc.* **1984**, *131* (12), No. 2737.
(46) Zheng, Y.; Chen, D.; Zhao, Y.; Bao, H.; Sun, Y. Elucidating the diffusion and interaction mechanisms of Zn2+ and H+ in MnO2 for aqueous zinc-ion batteries: A DFT study. *J. Power Sources* **2025**, *625*, No. 235658.
(47) Geng, C.; Sun, T.; Wang, Z.; Wu, J.-M.; Gu, Y.-J.; Kobayashi, H.; Yang, P.; Hai, J.; Wen, W. Surface-Induced Desolvation of Hydronium Ion Enables Anatase TiO2 as an Efficient Anode for Proton Batteries. *Nano Lett.* **2021**, *21* (16), 7021−7029.
(48) Holzapfel, N. P.; Augustyn, V.; Balland, V. Fundamentals of Proton-Insertion Coupled Electron Transfer (PICET) in Metal Oxides for Aqueous Batteries. *ACS Energy Lett.* **2025**, *10* (3), 1143−1164.
(49) Mateos, M.; Makivic, N.; Kim, Y.-S.; Limoges, B.; Balland, V. Accessing the Two-Electron Charge Storage Capacity of MnO2 in Mild Aqueous Electrolytes. *Adv. Energy Mater.* **2020**, *10* (23), No. 2000332.
(50) Godeffroy, L.; Aguilar, I.; Médard, J.; Larcher, D.; Tarascon, J.-M.; Kanoufi, F. Decoupling the Dynamics of Zinc Hydroxide Sulfate Precipitation/Dissolution in Aqueous Zn−MnO2 Batteries by Operando Optical Microscopy: A Missing Piece of the Mechanistic Puzzle. *Adv. Energy Mater.* **2022**, *12* (30), No. 2200722.
(51) Chen, H.; Dai, C.; Xiao, F.; Yang, Q.; Cai, S.; Xu, M.; Fan, H. J.; Bao, S.-J. Reunderstanding the Reaction Mechanism of Aqueous Zn−Mn Batteries with Sulfate Electrolytes: Role of the Zinc Sulfate Hydroxide. *Adv. Mater.* **2022**, *34* (15), No. 2109092.
(52) Chou, J.; Zhao, Y.; Li, X.-T.; Wang, W.-P.; Tan, S.-J.; Wang, Y.-H.; Zhang, J.; Yin, Y.-X.; Wang, F.; Xin, S.; Guo, Y.-G. Hydrogen Isotope Effects on Aqueous Electrolyte for Electrochemical Lithium-Ion Storage. *Angew. Chem., Int. Ed.* **2022**, *61* (25), No. e202203137.
(53) Dau, H.; Liebisch, P.; Haumann, M. X-ray absorption spectroscopy to analyze nuclear geometry and electronic structure of biological metal centers—potential and questions examined with special focus on the tetra-nuclear manganese complex of oxygenic photosynthesis. *Anal. Bioanal. Chem.* **2003**, *376* (5), 562−583.
(54) Hu, E.; Yu, X.; Lin, R.; Bi, X.; Lu, J.; Bak, S.; Nam, K.-W.; Xin, H. L.; Jaye, C.; Fischer, D. A.; et al. Evolution of redox couples in Li- and Mn-rich cathode materials and mitigation of voltage fade by reducing oxygen release. *Nat. Energy* **2018**, *3* (8), 690−698.
(55) Wu, F.; Gao, X.; Xu, X.; Jiang, Y.; Gao, X.; Yin, R.; Shi, W.; Liu, W.; Lu, G.; Cao, X. MnO2 Nanosheet-Assembled Hollow Polyhedron Grown on Carbon Cloth for Flexible Aqueous Zinc-Ion Batteries. *ChemSusChem* **2020**, *13* (6), 1537−1545.

https://doi.org/10.1021/acsami.5c22636
ACS Appl. Mater. Interfaces 2026, 18, 26078−26094

(56) Guo, X.; Zhou, J.; Bai, C.; Li, X.; Fang, G.; Liang, S. Zn/MnO2 battery chemistry with dissolution-deposition mechanism. *Mater. Today Energy* **2020**, *16*, No. 100396.
(57) Kao-Ian, W.; Tangthuam, P.; Kidkhunthod, P.; Limphirat, W.; Padchasri, J.; Aubert, N.; Ciatto, G.; In, I.; Wu, K. C.; Kheawhom, S. Monitoring Interfacial Dynamics of a Zinc-Ion Battery Cathode Using In Situ Grazing Incidence X-Ray Absorption Spectroscopy: A Case Study of Manganese Dioxide. *Small Methods* **2026**, *10*, No. e00871.
(58) Chen, H.; Dai, C.; Xiao, F.; Yang, Q.; Cai, S.; Xu, M.; Fan, H. J.; Bao, S. J. Reunderstanding the Reaction Mechanism of Aqueous Zn-Mn Batteries with Sulfate Electrolytes: Role of the Zinc Sulfate Hydroxide. *Adv. Mater.* **2022**, *34* (15), No. e2109092.
(59) Fairley, N.; Fernandez, V.; Richard-Plouet, M.; Guillot-Deudon, C.; Walton, J.; Smith, E.; Flahaut, D.; Greiner, M.; Biesinger, M.; Tougaard, S.; et al. Systematic and collaborative approach to problem solving using X-ray photoelectron spectroscopy. *Appl. Surf. Sci. Adv.* **2021**, *5*, No. 100112.
(60) Prescher, C.; Prakapenka, V. B. DIOPTAS: a program for reduction of two-dimensional X-ray diffraction data and data exploration. *High Pressure Res.* **2015**, *35* (3), 223−230.
(61) Newville, M. Larch: An Analysis Package for XAFS and Related Spectroscopies. *J. Phys.: Conf. Ser.* **2013**, *430*, No. 012007.
(62) Gürsoy, D.; De Carlo, F.; Xiao, X.; Jacobsen, C. TomoPy: a framework for the analysis of synchrotron tomographic data. *J. Synchrotron Radiat.* **2014**, *21* (5), 1188−1193.
(63) Dowd, B.; Campbell, G.; Marr, R.; Nagarkar, V.; Tipnis, S.; Axe, L.; Siddons, D. In *Developments in Synchrotron X-ray Computed Microtomography at the National Synchrotron Light Source*, SPIE Proceedings; SPIE, 1999.
(64) Ge, M.; Lee, W.-K. PyXAS−an open-source package for 2D X-ray near-edge spectroscopy analysis. *J. Synchrotron Radiat.* **2020**, *27* (2), 567−575.
(65) Ravel, B.; Newville, M. ATHENA, ARTEMIS, HEPHAESTUS: data analysis for X-ray absorption spectroscopy using IFEFFIT. *J. Synchrotron Radiat.* **2005**, *12* (4), 537−541.

https://doi.org/10.1021/acsami.5c22636
ACS Appl. Mater. Interfaces 2026, 18, 26078−26094